Thermal conductivity at the bottom of the Earth's lower mantle: measurements of pyrolite up to 120 GPa and 2500 K

Zachary M. Geballe[a,*], Nathan Sime[b], James Badro[c], Peter E. van Keken[b], Alexander F. Goncharov[a]

[a] *Geophysical Laboratory, Carnegie Institution for Science, Washington DC, USA*
[b] *Department of Terrestrial Magnetism, Carnegie Institution for Science, Washington DC, USA*
[c] *Institute de Physique du Globe, Paris, France*

Abstract

Knowledge of thermal conductivity of mantle minerals is crucial for understanding heat transport from the Earth's core to mantle. At the pressure-temperature conditions of the Earth's core-mantle boundary, calculations of lattice thermal conductivity based on atomistic models have determined values ranging from 1 to 14 W/m/K for bridgmanite and bridgmanite-rich mineral assemblages. Previous studies have been performed at room temperature up to the pressures of the core-mantle boundary, but correcting these to geotherm temperatures may introduce large errors. Here we present the first measurements of lattice thermal conductivity of mantle minerals up to pressures and temperatures near the base of the mantle, 120 GPa and 2500 K. We use a combination of continuous and pulsed laser heating in a diamond anvil cell to measure the lattice thermal conductivity of pyrolite, the assemblage of minerals expected to make up the lower mantle. We find a value of $3.9^{+1.4}_{-1.1}$ W/m/K at 80 GPa and 2000 to 2500 K and $5.9^{+4.0}_{-2.3}$ W/m/K at 124 GPa and 2000 to 3000 K. This rules out the highest calculations of thermal conductivity of the Earth's mid-lower mantle (i.e. $k < 6$ W/m/K at 80 GPa), but is consistent with both the high and low calculations of thermal conductivity near the base of the lower mantle.

Keywords: Earth's heat loss, diamond anvil cell, finite element methods

*Corresponding author
Email addresses: zgeballe@carnegiescience.edu (Zachary M. Geballe), nsime@carnegiescience.edu (Nathan Sime), badro@ipgp.fr (James Badro), pvankeken@carnegiescience.edu (Peter E. van Keken), agoncharov@carnegiescience.edu (Alexander F. Goncharov)

1. Introduction

It is estimated that up to 16 TW of heat flows from the Earth's core into the overlying mantle (Pozzo et al., 2012). Heat transfer across the base of the mantle is the rate limiting step of how much heat is extracted from the core and thereby controls the dynamics of the Earth's core, the generation of its magnetic field, and the energy budget of mantle convection. One key factor that influences the magnitude of core-mantle boundary (CMB) heat flux is the thermal conductivity of the assemblage of minerals that makes up the lowermost mantle, which can be approximated as 75% bridgmanite, 19% ferropericlase and 6% $CaSiO_3$ perovskite (Stackhouse et al., 2015). Determining the thermal conductivity of these minerals at the high pressure and temperature is therefore a crucial step in understanding the core-mantle heat flux and its many ramifications on dynamics of the deep Earth.

The lattice thermal conductivity of bridgmanite has been calculated using a variety of classical- and quantum-mechanics based methods, providing a key starting point for calculation of pyrolite's thermal conductivity. The discrepancies between results from different research groups are large. At 120 GPa and 2500 K, for example, five recent studies calculate thermal conductivity of $MgSiO_3$ bridgmanite to be 1, 5, 6.5, 9.5, and 14 W/m/K (Tang et al., 2014; Dekura et al., 2013; Stackhouse et al., 2015; Ammann et al., 2014; Haigis et al., 2012). A sixth study extrapolates to 8.3 W/m/K upon scaling from 300 K to 2500 K (Ghaderi et al., 2017).

The discrepancies reduce somewhat when estimating total conductivity for pyrolite by adding bridgmanite's radiative thermal conductivity and averaging with conductivities of ferropericlase and calcium perovskite. For example, Tang et al. (2014) estimates 3.5 W/m/K total conductivity whereas Stackhouse et al. (2015) estimates 10 W/m/K at 125 GPa and 2500 K.

Laboratory measurements of lattice thermal conductivity of mantle minerals have been conducted up to the pressure of the core-mantle boundary, but measurements at pressure above 40 GPa have always been at (or near) room temperature (300 to 500 K). Two different research groups measured conductivity of bridgmanite to be 15 to 25 W/m/K at 120 GPa and room temperature, with conductivity decreasing with increasing Fe or Al substitution (Ohta et al., 2012; Okuda et al., 2017; Hsieh et al., 2017). One high-temperature study of thermal conductivity of bridgmanite reached the pressure of the uppermost lower mantle, and measured 8 W/m/K at 1070 K for pure $MgSiO_3$ and 4 W/m/K for $Mg_{0.97}Fe_{0.03}SiO_3$ (Manthilake et al., 2011). Laboratory measurements have also been made on lattice thermal conductivity of ferropericlase to CMB pressures at room temperature (Dalton et al., 2013; Imada et al., 2014; Goncharov et al., 2015; Hsieh et al., 2018), of MgO to 32 GPa and 2500 K (Goncharov et al., 2009), and of the pressure derivative of MgO up to 40 GPa and 2000 K (Rainey and Kavner, 2014). Radiative thermal conductivity has been experimentally shown to be relatively small (< 1 W/m/K) even at high temperatures (Lobanov et al., 2017, 2019a,b)

Overall, published experimental determinations of lattice thermal conductivity provide a starting point for estimating thermal conductivity at the base of the Earth's mantle, but large extrapolation is required to reach the appropriate conditions of pressure and temperature.

To date, no laboratory measurements have been reported for thermal conductivity of bridgmanite, ferropericlase, or Ca-perovskite at pressures and temperatures simultaneously above 40 GPa and

500 K. The reason is the extreme challenge of maintaining a stable high temperature state while quickly heating part of the sample and measuring the time-dependent response as heat flows through the sample.

Here we present the first measurements of thermal conductivity of pyrolite at several pressures and temperatures along the Earth's geotherm from 40 to 124 GPa at 1900 to 2900 K. These measurements combine several cutting-edge techniques: pulsed and continuous laser-heating, time-resolved temperature measurements, double-sided iridium coating of thin samples, and finite element modeling of heat flow in a diamond anvil cell.

2. Methods

2.1. Experimental Methods

We present the results of five high pressure runs in laser-heated diamond anvil cells. In each run, an iridium-coated pyrolite sample is compressed, laser heated to ∼2000 K, and pulsed laser heated from one side. Thermal emissions are collected as a function of time and space, and are analyzed to determine thermal conductivity of the pyrolite sample.

Each diamond cell is loaded with a ∼6 μm-thick slab of pyrolite glass coated with 2 nm of titanium and 43 ± 5 or 178 ± 5 nm of iridium, surrounded by potassium-chloride or argon, and pressed inside the hole of a rhenium gasket. The titanium serves as an adhesion layer to prevent the iridium from delaminating prior to the high pressure run. The first set of experiments used the thinner iridium coating, which may have contributed to failure of several experiments not reported here, in which holes formed in the iridium layer upon pulsed heating. The thicker coating was used for the second set of experiments. The potassium-chloride or argon serves as the pressure medium and thermal insulation from the diamonds. In the case of argon, the iridum-pyrolite-iridium sandwich was placed atop three ruby spheres before gas-loading in order to separate it from one diamond. The pyrolite glass is the same one used in previous measurements of radiative conductivity (Lobanov et al., 2019a). It was synthesized by grinding together $CaCO_3$, MgO, Al_2O_3, SiO_2 and Fe_2O_3, decarbonating at 850 °C and fusing in a laser levitation furnace at 2000 °C in a gas with oxygen fugacity 0.7 log units above the iron-wüstite buffer; see (Lobanov et al., 2019a) for details. The glass's chemical composition was measured by (Lobanov et al., 2019a) to be 38.15±0.12 wt% MgO, 46.6±0.1 wt% SiO_2, 2.16±0.03 wt% CaO, 8.66 ± 0.12 wt% FeO, and 4.24 ± 0.06 wt% Al_2O_3.

The subsequent compression and heating procedure is similar to that presented in McWilliams et al. (2015) and Konôpková et al. (2016). Samples are compressed to the desired pressure, heated to ∼2500 K to convert the glass starting material to a polycrystalline assemblage of minerals (bridgmanite, ferropericlase, calcium-perovskite), and pulsed-heated from one side while measuring time-resolved thermal emissions on a streak camera and spatially-resolved thermal emissions on a CCD camera. Several sets of thermal emissions data are collected from each side to make sure temperatures do not drift substantially through time. This also ensures that there is no residual amorphous material near the hotspot that continues to crystallize during the experiment The samples are decompressed to ambient

pressure, cross sections are cut with a focused ion beam, thickness is measured, and chemical composition is mapped in a SEM. Fig. 1 shows an example of a compressed sample and its cross section after decompression. Further details are presented in the Supplementary Material.

2.2. Data analysis

We divide the analysis into data reduction, finite element modeling, and error analysis. In the first step, the raw data is reduced to determine temperature as a function time and location on the two iridium surfaces. Then a finite element model is used to find best-fit values of thermal conductivity of the pyrolite sample, k_{pyro}, and the insulating medium, k_{ins}, while fixing all other parameters to their estimated values. Finally, all parameters are co-varied with k_{pyro} and k_{Ir} is co-varied with both k_{pyro} and k_{ins} to determine the uncertainty in pyrolite's thermal conductivity, $\sigma_{k_{\mathrm{pyro}}}$.

2.2.1. Data reduction

Each image from the streak camera is reduced to normalized temperature as a function of time in a five step process. First, measured intensity is corrected for geometrical distortion in the streak tube. Second, it is corrected for bias in the conversion efficiency from emitted photon to measured intensity. The bias is both in time and wavelength, and is corrected with a reference image from a tungsten lamp heated to a known temperature. Third, the Planck function is fit to intensity averaged over a relatively wide time-window (3 or 10 μs) using both temperature and emissivity as fitting parameters. Fourth, emissivity is fixed to the value from the third step and the Planck function is fit to the intensity averaged over a set of narrow time-slices. For example, Planck fits to forty slices of 0.5 μs width generate the $\sim$20 μs-duration temperature-time curves in Fig. S4. The fifth step is reduction to a normalized temperature, which enables efficient comparison of measurements to each other and to finite element models. This normalization has no effect on the model parameters needed to match the data, besides the parameter describing the magnitude of laser power.

In addition to measuring the temporal evolution of temperature, the spatial distribution of thermal emissions from the CCD image are reduced to temperature versus distance. Briefly, we reference the peak intensity on the CCD camera to the temperature measured on the streak camera prior to heating pulses. We then use the Planck function to determine $T(x)$. This analysis gives us the width of the hotspot, T_{FWHM}, which is an important input for the finite element model used to infer thermal conductivity. Here, 'FWHM' means the full width at half the maximum temperature above the 300 K baseline temperature. Details are described in the Supplementary Material.

2.2.2. Finite element modeling

Computational modeling is required to determine the thermal conductivity of our samples, because we lack an analytical model to the three-dimensional heat flow of this experiment. We solve the governing heat equation using finite element modeling based on the FEniCS project (Alnæs et al., 2015). We model the diamond anvil assembly with an axisymmetric geometry with rotational symmetry around the center of the assembly. We assume 300 K Dirichlet boundary conditions at $r = 100$ μm and $z = \pm 40$ μm, where r is radius from the center and z is the axial distance from the center of the

sample (Fig. 2). Thicknesses of sample and insulation match those measured in each experiment. As in Hsieh et al. (2017), we assume the volume of the iridium coating varies with pressure according to its equation of state and that its surface area matches that of the sample. In other words, the iridium adheres perfectly to the sample as the sample flattens under pressure. This means the iridium thins by 5 to 10% less than the sample due to the fact that iridium is less compressible than pyrolite. All thicknesses are listed in Table 1. An example of the finite element mesh is shown in Fig. S6.

The free parameters in this model are thermal conductivities of pyrolite, iridium and the insulator (KCl or Ar). To restrict the parameter space that must be explored, we assume the lower bound $k_{\mathrm{Ir}} > 30$ W/m/K (see Supplement for details). All other model parameters are either measured in this study (such as the parameters describing the geometry), measured in other studies (density), assumed (heat capacity), or are considered to negligibly affect the modeled temperature evolution of the iridium surfaces (such as the thermal conductivity of the gasket and diamond, and the distance to boundaries of the modeled domain). The < 2 nm thick titanium adhesion layer is not modeled, since it is much thinner than the iridium layer and has similar conductive properties, meaning it provides negligible resistance to axial heat flow, negligible heat capacity, and negligible radial conductance.

In reality, all three free parameters, k_{pyro}, k_{Ir}, and k_{ins}, depend on temperature, but we do not model their temperature-dependencies here. Instead, our main results are the values of k_{pyro} that are consistent with our data at each pressure, P, and range of temperatures, $T \pm \sigma_T$; see Fig. 4b and Table 2 for values of P, T, σ_T, and estimated pressure uncertainty, σ_P.

We model the background and pulse heating with two different methods in our determination of k_{pyro} and its uncertainty. Both methods solve the heat equation on the same domain, but they differ in one important way. 'Method Q' includes a heating term Q on the pulsed-side iridium surface, $Q(r,t) = Q_0(r)(1 + dQ(t))$, where t is time, Q_0 is a background term, and dQ is the time-dependent heating pulse. In 'method T' we impose a time-dependent Dirichlet boundary condition at the pulsed-side iridium surface, $T(r,t) = 300 + T_0(r)(1 + dT(t))$, where T is absolute temperature in K, T_0 is a background term, and dT describes the effect of the pulse heating. Method Q models the thermal evolution that is closer to the reality we expect: the spatial distribution of absorbed laser power remains constant throughout the heating pulse. Method T models the case of a constant spatial distribution of temperature, but in reality we expect a slight widening of the temperature distribution throughout the duration of the pulse. The two methods result in best fit values of k_{pyro} within 5% of each other for four of our six data points, and up to 25% for the data points at 40 and 68 GPa. The comparison of results obtained with these two methods is provided in Table S1 and the implementation of the methodologies is further described in the Supplementary Information.

We use the two methods in the following sequence. First, we use method T to fit measurements of temperature vs. time and temperature vs. distance. In this step we assume the values of k_{Ir} listed in Table 1 and fit for k_{pyro} and k_{ins}. Second, we remove the assumption of k_{Ir} and search for all values of (k_{pyro}, k_{Ir}, k_{ins}) that fit the data. From this search, along with uncertainty propagation from all other parameters (as describe in the Supplementary Material), we determine the uncertainty $\sigma^T_{k_{\mathrm{pyro}}}$. Third, we use these results as a starting point to find the best-fit of the conductivity k^Q_{pyro} with method

Q. Examples of best-fit models of method Q to data from 80 GPa data is shown in Fig. 3. Finally, we assume the uncertainty in results obtained with method Q is proportional to that determined in method T, that is $\sigma^Q_{k_{\rm pyro}} = \sigma^T_{k_{\rm pyro}} k^Q_{\rm pyro}/k^T_{\rm pyro}$. We avoid searching the parameter space to determine $\sigma^Q_{k_{\rm pyro}}$ explicitly, because the computational effort needed for method Q is significantly larger than that for method T for reasons described in the Supplementary Material. The final results $k^Q_{\rm pyro}$ and $\sigma^Q_{k_{\rm pyro}}$ are reported without the superscript "Q" in all summary figures and Table 2.

Uncertainty in $\sigma^T_{k_{\rm pyro}}$ is determined by quadrature addition of uncertainties from: (i) the range of values of $k_{\rm pyro}$ that fit the data when exploring the three-dimensional parameter space $\mathbf{k} = (k_{\rm pyro}, k_{\rm ins}, k_{\rm Ir})$; and (ii) uncertainty propagated from uncertainty in seven measured or theoretically estimated parameters. These seven parameters are pyrolite thickness, iridium thickness, other-side insulator thickness, FWHM of spatial distribution of temperature, and ρc_v of pyrolite, iridium, and the insulator. All other model parameters have minimal effect on the best-fit value of $k_{\rm pyro}$. Table S1 lists all uncertainties.

3. Results and Discussion

The newly determined thermal conductivity of pyrolite is between 3 and 10 W/m/K at all pressures from 40 to 124 GPa (Fig. 4). This is consistent with both the low and high calculations of thermal conductivity of pyrolite near the base of the lower mantle, but does not permit any estimates lower than those of Tang et al. (2014) or higher than those of Stackhouse et al. (2015). At shallower depths, near the middle of the lower mantle, our most precise datum rules out the conductivity calculations with $k_{\rm pyro} > 6$ W/m/K (Stackhouse et al., 2015). At even lower pressures, our 40 GPa data rule out the conductivity calculations with $k_{\rm pyro} < 3.5$ W/m/K (Tang et al., 2014).

While our data are consistent with previous laboratory measurements of bridgmanite at lower pressure and/or temperature, comparisons are complicated by differences in sample composition (Fig. 5). The conductivity of Fe-bearing bridgmanite at 26 GPa and 1000 K was measured by Manthilake et al. (2011) to be 4 W/m/K, which matches our measurements of pyrolite at 40 and 41 GPa within the error bars. Indeed, we expect little change overall since the higher temperatures studied here reduce the conductivity of Fe-bearing bridgmanite by a few tens of percent, and the addition of magnesiowüstite likely increases it by a few tens of percent. Compared to the room temperature experimental data of Fe-bearing bridgmanite (Hsieh et al., 2017), the approximately two-fold lower thermal conductivity measured here suggests that the effect of heating from 300 to 2500 K, which likely decreases k, outweighs the addition of ferropericlase, which likely increases k.

Our results suggest that the pressure dependence of thermal conductivity is relatively small, and that it could be either positive or negative. Assuming a linear dependence on pressure over the range 40 to 124 GPa, the slope $dk_{\rm pyro}/dP$ is estimated to be between -0.04 and +0.04 W/m/K/GPa. Even the greatest values in this range are less than slopes for the theoretically-determined conductivities of pyrolite in Stackhouse et al. (2015) ($dk/dP = 0.06$) and for bridgmanite in four other studies (Dekura et al., 2013; Haigis et al., 2012; Ghaderi et al., 2017; Ammann et al., 2014), but in agreement

with the pressure-derivative calculated for bridgmanite in Tang et al. (2014). In all cases, we are comparing values of dk/dP along the 2500 K isotherm. The relatively small slope measured here is broadly consistent with the room-temperature measurements of Fe-bearing bridgmanite of Hsieh et al. (2017), which show $dk_{\mathrm{pyro}}/dP \sim 0.03$ W/m/K/GPa at pressures above 40 GPa. More detailed analysis of pressure trends awaits further data. The possible influence of the spin-transition is especially intriguing, as suggested by Hsieh et al. (2017).

Our highest pressure data point at 124 GPa and 2100 to 2800 K constrains the thermal conductivity near the base of the mantle to the range 3–10 W/m/K. The lower end of this range overlaps with the theory-based estimate of Tang et al. (2014), while the upper limit of this range is slightly lower than the lowest estimate of Stackhouse et al. (2015).

The thermal conductivity of the lowermost mantle is one piece of a complicated puzzle that needs to be solved to better understand the dynamics of the Earth's mantle and core-mantle interaction. The cooling of the core is largely dominated by the ability of the lower mantle to absorb the heat flowing from the core, which in turn is controlled by the thermal conductivity, temperature gradients, and speed of convective flow of the lowermost mantle. The speed of convective flow is determined by rheology combined with thermal and chemical buoyancy forces. Our current understanding of lower mantle rheology is mostly incomplete except for possible inferences of the broad viscosity structure from geodetic and geodynamic observations (e.g., Mitrovica and Forte, 1997; Rudolph et al., 2015; Lau et al., 2016). One source of buoyancy is the thermal expansion of mantle material in proximity to the Earth's hot core. Other sources are also likely, including density differences associated with deep mantle structures that have been identified seismically by low shear wave velocities. An understanding of whether these structures are largely static or highly dynamic is critical for determining the mantle's ability to absorb core heat flow (Nakagawa and Tackley, 2014).

It is possible to construct an understanding of core heat flow and its connection to heat transport from the deep mantle from assumptions of the thickness of and temperature contrast across the thermal boundary layer (Tang et al., 2014; Stackhouse et al., 2015) but uncertainties are large (see, e.g., Figure 5 in Tang et al., 2014). A simple calculation shows the inherent impact due to multiplication of these uncertainties. If we assume a range of core heat flow, $Q = 7$ to 15.5 TW, a range of thermal conductivity, $k = 3$ to 10 W/m/K, and a temperature jump across the thermal boundary layer, $\Delta T = 600$ to 2000 K, then we would determine a thermal boundary layer thickness, δ, that is between 32 and 360 km by using the equation

$$Q = \frac{k \Delta T A_{\mathrm{CMB}}}{\delta}$$

where $A_{\mathrm{CMB}} = 1.5 \times 10^{14}$ m^2 is the surface area of the core-mantle boundary. To arrive at a more precise prediction, we clearly need a significant reduction in the uncertainties of the governing parameters including the thermal conductivity.

It remains critically important to continue to improve our understanding about material properties of the deep Earth as the combination of high-pressure petrological studies, geodynamical model simulations, and quantitative comparisons with seismological observations and models (e.g., Ritsema

et al., 2007; Jones et al., in revision) should eventually allow us to develop a deep understanding of the way the planet loses its internal heat.

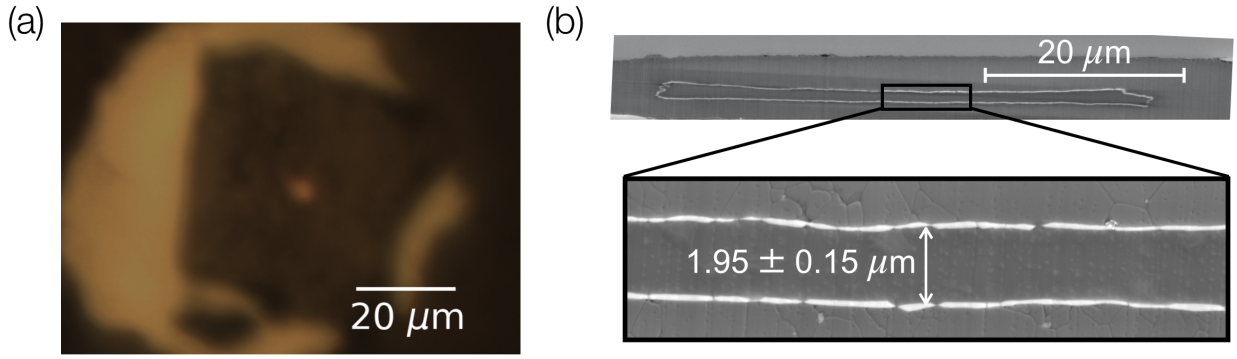

Figure 1: (a) Iridium-coated pyrolite sample heated at 80 GPa. The hot spot is the white spot in the middle. The sample is illuminated from the back and front by white light. (b) Secondary electron image of cross section of the iridium-coated pyrolite sample surrounded with KCl, recovered from 80 GPa, covered in a tungsten protection layer (light grey) and sliced in half by a focused ion beam.

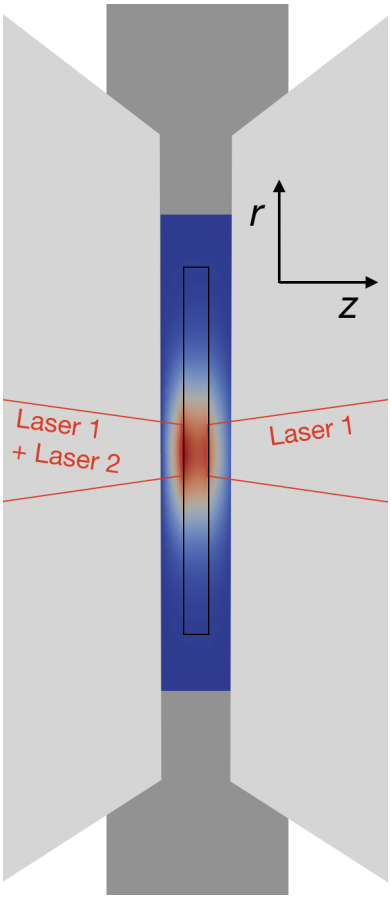

Figure 2: Experimental setup for thermal conductivity measurements. An iridium-coated slab of pyrolite (black outline) is heated from both sides by a continuous laser (Laser 1) and from the "pulsed side" by a pulsed laser (Laser 2). Thermal insulation separates the sample from the diamond culets (light grey) and gasket (dark grey). Blue to red shading represent simulated temperatures of pyrolite, iridium, and insulation from 300 K (blue) to 2500 K (red).

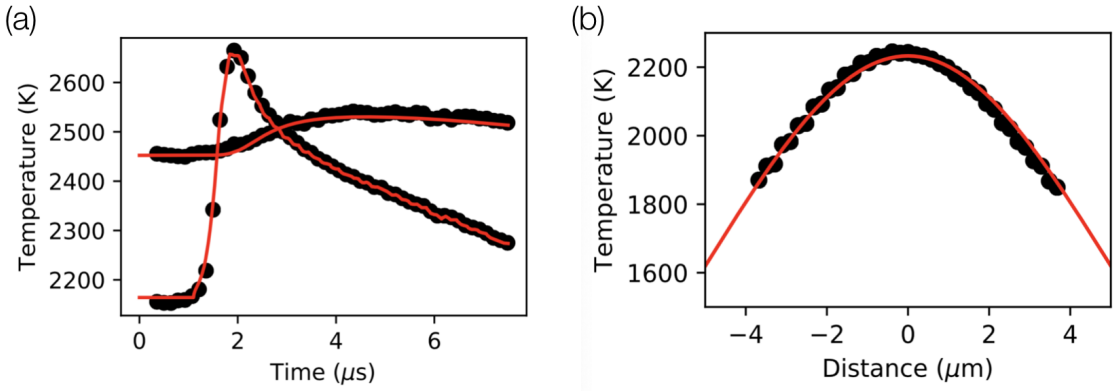

Figure 3: Example of measurements and fits at 80 GPa. (a) Temperature vs. time on pulsed-heated side (2100 to 2700 K curve) and other side (2450 to 2550 K curve). (b) Temperature vs. distance from center of hotspot on pulsed-heated side at the time corresponding to 0 μs in (a).

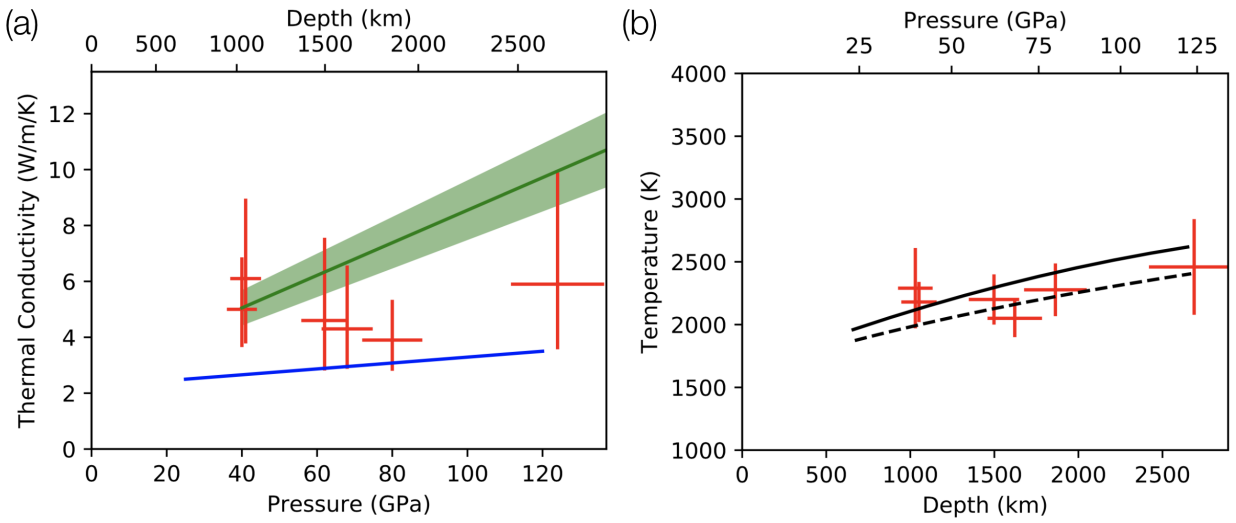

Figure 4: (a) Thermal conductivity of pyrolite at 1900 to 2900 K. Experimental data from this study (red symbols). Theoretical calculations from Stackhouse et al. (2015) (interpolated to 2500 K; green) and from Tang et al. (2014) (extrapolated to their estimated geotherm ranging from 2000 to 2500 K; blue). (b) Temperature of data points presented here (red) as a function of depth along with the estimated lower mantle geotherms of Katsura et al. (2010) (solid black) and Brown and Shankland (1981) (dashed black).

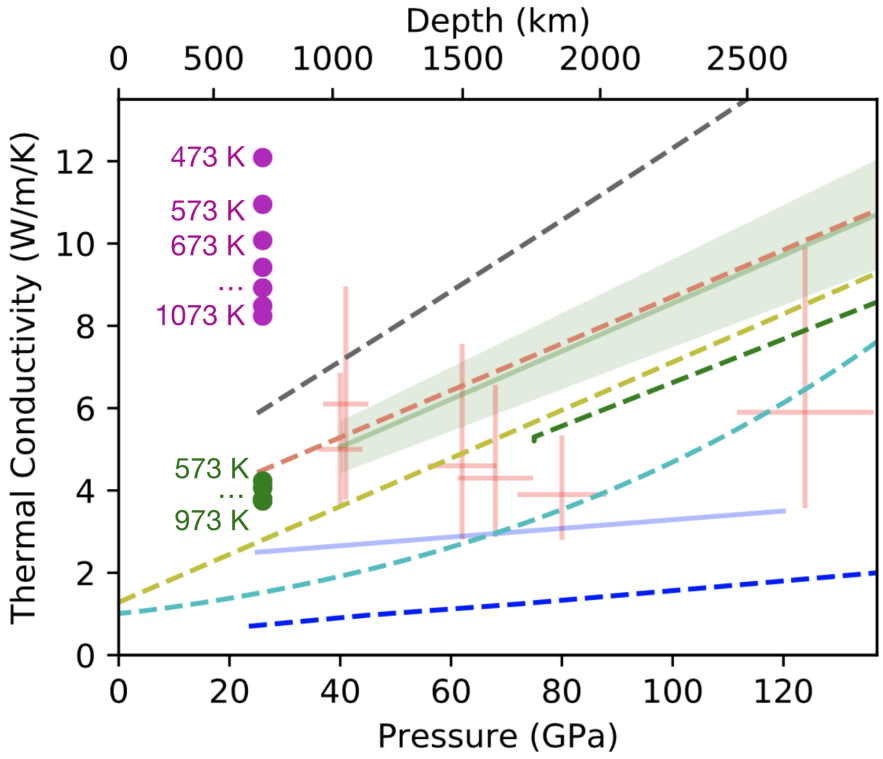

Figure 5: Thermal conductivity of pyrolite and bridgmanite at 1900 to 2900 K, except where noted to be < 1900 K. Pyrolite is represented as in Fig. 4: red are our experimental data; green is from Stackhouse et al. (2015); and blue is from Tang et al. (2014). Bridgmanite experimental data at 470 to 1070 K of Manthilake et al. (2011) are shown by magenta circles ($MgSiO_3$ bridgmanite) and green circles ($Mg_{0.97}Fe_{0.03}SiO_3$ bridgmanite). Calculations interpolated to 2500 K for $MgSiO_3$ bridgmanite are shown as dashed lines: Haigis et al. (2012) in grey, Ammann et al. (2014) in orange; Ghaderi et al. (2017) in yellow; Stackhouse et al. (2015) in green; Dekura et al. (2013) in cyan; Tang et al. (2014) in blue).

Run	P (GPa)	ρ (kg/m^3)			c_v (J/m^3/kg)			k (W/m/K)	T_{FWHM} (μm)	d_{pyro} (μm)	d_{Ir} (μm)	$d_{\mathrm{ins,pside}}$ (μm)	$\mathrm{d}_{\mathrm{ins,oside}}$ (μm)	ins. material	n_{ins}
		pyrolite	Ir	insulator	pyrolite	Ir	insulator	Ir							
1	40	4676	24781	4556	1158	130	623	278	9.5	2.47	0.098	7.7	6	Ar	1.9
2	41	4689	24822	3488	1158	130	668	280	12	2.85	0.025	9.9	8.8	KCl	1.9
3	62	4944	25767	3860	1158	130	668	318	10	2.5	0.078	3.2	6.4	KCl	2
4	68	5019	27136	3957	1158	130	668	330	18	1.4	0.019	5.7	5.8	KCl	2
4	80	5164	26504	4131	1158	130	668	352	13.2	1.84	0.062	3.2	6.3	KCl	2.05
5	124	5573	27136	4671	1158	130	668	433	8.5	1.7	0.039	1.6	2.1	KCl	2.16

Table 1: Key inputs to the finite element model used to infer thermal conductivity of pyrolite. Iridium thermal conductivity is used as a starting guess and is an assumption for the best fit, k_{pyro}, but not for uncertainty analysis. Insulator refractive index, n_{ins}, at room temperature is used to determine thicknesses of insulation on each side of the sample, $d_{\mathrm{ins,pside}}$ and $d_{\mathrm{ins,oside}}$, assuming the values from from Goncharov (unpublished) for KCl and Chen et al. (2010) for Ar.

				Pyrolite				Insulator			Iridium	
P	σ_P	T	σ_T	$k_{\rm pyro}$	σ_k^-	σ_k^+	$D_{\rm pyro}$	$k_{\rm ins}$	$k_{\rm ins}^{\rm max}$	ins.	$k_{\rm Ir}$	$k_{\rm Ir}^{\rm max}$
(GPa)		(K)		(W/m/K)			(mm^2/s)	(W/m/K)		material	(W/m/K)	
40	4	2290	320	5	-1.4	+1.9	0.92	2	5.7	Ar	278	600
41	4.1	2180	160	6.1	-2.3	+2.9	1.12	3	8.9	KCl	280	1600
62	6.2	2200	200	4.6	-1.8	+3	0.8	12.6	20.1	KCl	318	1300
68	6.8	2050	150	4.3	-1.4	+2.3	0.74	4.1	6.6	KCl	330	1400
80	8	2280	210	3.9	-1.1	+1.4	0.65	10	18.2	KCl	352	1300
124	12.4	2460	380	5.9	-2.3	+4	0.91	10.1	12.5	KCl	433	2000

Table 2: Results of finite element analysis. Best fits, $k_{\rm pyro}$ and $k_{\rm ins}$, assume listed values of $k_{\rm Ir}$. Uncertainties, σ_k, and upper-bounds, $k^{\rm max}$, do not assume any particular value of $k_{\rm Ir}$.

4. Acknowledgments

We thank Suzy Vitale for performing the FIB milling, Emma Bullock for assistance with the SEM analysis, and Nick Holtgrewe for computer codes to reduce streak camera data. This project was sponsored by a Carnegie Venture Postdoctoral Fellowship to ZMG.

References

Akahama, Y., Kawamura, H., 2006. Pressure calibration of diamond anvil Raman gauge to 310 GPa. J. Appl. Phys. 100, 043516. doi:10.1063/1.2335683.

Alnæs, M.S., Blechta, J., Hake, J., Johansson, A., Kehlet, B., Logg, A., Richardson, C., Ring, J., Rognes, M.E., Wells, G.N., 2015. The FEniCS Project Version 1.5. Archive of Numerical Software 3, 9–23. doi:10.11588/ans.2015.100.20553.

Amestoy, P.R., Duff, I.S., L'Excellent, J.Y., 2000. Multifrontal parallel distributed symmetric and unsymmetric solvers. Computer Methods in Applied and Mechanical Engineering 184, 501–520. doi:10.1016/S0045-7825(99)00242-X.

Ammann, M.W., Walker, A.M., Stackhouse, S., Wookey, J., Forte, A.M., Brodholt, J.P., Dobson, D.P., 2014. Variation of thermal conductivity and heat flux at the Earth's core mantle boundary. Earth and Planetary Science Letters 390, 175–185. doi:10.1016/j.epsl.2014.01.009.

Balay, S., Abhyankar, S., Adams, M.F., Brown, J., Brune, P., Buschelman, K., Dalcin, L., Eijkhout, V., Gropp, W.D., Kaushik, D., Knepley, M.G., May, D.A., McInnes, L.C., Mills, R.T., Munson, T., Rupp, K., Sanan, P., Smith, B.F., Zampini, S., Zhang, H., Zhang, H., 2019. PETSc Web page. URL: `http://www.mcs.anl.gov/petsc`.

Brown, J.M., Shankland, T.J., 1981. Thermodynamic parameters in the Earth as determined from seismic profiles. Geophysical Journal International 66, 579–596. doi:10.1111/j.1365-246X.1981.tb04891.x.

Cagran, C., Pottlacher, G., 2007. Thermophysical properties and normal spectral emittance of iridium up to 3500 K. International Journal of Thermophysics 28, 697–710. doi:10.1007/s10765-007-0188-9.

Chen, B., Gleason, A.E., Yan, J.Y., Koski, K.J., Clark, S., Jeanloz, R., 2010. Elasticity, strength, and refractive index of argon at high pressures. Physical Review B 81, 144110. doi:10.1103/PhysRevB.81.144110.

Dalton, D.A., Hsieh, W.P., Hohensee, G.T., Cahill, D.G., Goncharov, A.F., 2013. Effect of mass disorder on the lattice thermal conductivity of MgO periclase under pressure. Scientific Reports 3, 2400. doi:10.1038/srep02400.

Dekura, H., Tsuchiya, T., Tsuchiya, J., 2013. Ab initio lattice thermal conductivity of $MgSiO_3$ perovskite as found in Earth's lower mantle. Physical Review Letters 110, 025904. doi:10.1103/PhysRevLett.110.025904.

Dewaele, A., Belonoshko, A.B., Garbarino, G., Occelli, F., Bouvier, P., Hanfland, M., Mezouar, M., 2012. High-pressure-high-temperature equation of state of KCl and KBr. Physical Review B 85, 214105. doi:10.1103/PhysRevB.85.214105.

Errandonea, D., Boehler, R., Japel, S., Mezouar, M., Benedetti, L.R., 2006. Structural transformation of compressed solid Ar: An x-ray diffraction study to 114 GPa. Physical Review B 73, 092106. doi:10.1103/PhysRevB.73.092106.

Geuzaine, C., Remacle, J.F., 2009. Gmsh: A 3-D finite element mesh generator with built-in pre- and post-processing facilities. International Journal for Numerical Methods in Engineering 79, 1309–1331. doi:doi.org/10.1002/nme.2579.

Ghaderi, N., Zhang, D.B., Zhang, H., Xian, J., Wentzcovitch, R.M., Sun, T., 2017. Lattice thermal conductivity of $MgSiO_3$ perovskite from first principles. Scientific Reports 7, 5417. doi:10.1038/s41598-017-05523-6.

Goncharov, A.F., Beck, P., Struzhkin, V.V., Haugen, B.D., Jacobsen, S.D., 2009. Thermal conductivity of lower-mantle minerals. Physics of the Earth and Planetary Interiors 174, 24–32. doi:10.1016/j.pepi.2008.07.033.

Goncharov, A.F., Lobanov, S.S., Tan, X., Hohensee, G.T., Cahill, D.G., Lin, J.F., Thomas, S.M., Okuchi, T., Tomioka, N., 2015. Experimental study of thermal conductivity at high pressures: Implications for the deep Earth's interior. Physics of the Earth and Planetary Interiors 247, 11–16. doi:10.1016/j.pepi.2015.02.004.

Haigis, V., Salanne, M., Jahn, S., 2012. Thermal conductivity of MgO, $MgSiO_3$ perovskite and post-perovskite in the Earth's deep mantle. Earth and Planetary Science Letters 355–356, 102 – 108. doi:10.1016/j.epsl.2012.09.002.

Hsieh, W.P., Deschamps, F., Okuchi, T., Lin, J.F., 2017. Reduced lattice thermal conductivity of Fe-bearing bridgmanite in earth's deep mantle. Journal of Geophysical Research: Solid Earth 122, 4900–4917. doi:10.1002/2017JB014339.

Hsieh, W.P., Deschamps, F., Okuchi, T., Lin, J.F., 2018. Effects of iron on the lattice thermal conductivity of Earth's deep mantle and implications for mantle dynamics. Proceedings of the National Academy of Sciences 115, 4099–4104. doi:10.1073/pnas.1718557115.

Imada, S., Ohta, K., Yagi, T., Hirose, K., Yoshida, H., Nagahara, H., 2014. Measurements of lattice thermal conductivity of MgO to core-mantle boundary pressures. Geophysical Research Letters 41, 4542–4547. doi:10.1002/2014GL060423.

Jones, T., Maguire, R., van Keken, P., Ritsema, J., in revision. Subducted oceanic crust as the origin of lower-mantle structures. Progress in the Earth and Planetary Sciences .

Katsura, T., Yoneda, A., Yamazaki, D., Yoshino, T., Ito, E., 2010. Adiabatic temperature profile in the mantle. Physics of the Earth and Planetary Interiors 183, 212 – 218. doi:10.1016/j.pepi.2010.07.001. special Issue on Deep Slab and Mantle Dynamics.

Konôpková, Z., McWilliams, R.S., Gómez-Pérez, N., Goncharov, A.F., 2016. Direct measurement of thermal conductivity in solid iron at planetary core conditions. Nature 534, 99–101. doi:10.1038/nature18009.

Lau, H., Mitrovica, J., Austermann, J., Crawford, O., Al-Attar, D., Latychev, K., 2016. Inferences of mantle viscosity based on ice age data sets: Radial structure. Journal of Geophysical Research: Solid Earth 121, 6991–7012. doi:10.1002/2016JB013043.

Lobanov, S., Holtgrewe, N., Ito, G., Badro, J., Piet, H., Nabiei, F., Lin, J., Bayarjargal, L., Wirth, R., Schriber, A., Goncharov, A., 2019a. Blocked radiative heat transport in the hot pyrolitic lower mantle URL: `https://arxiv.org/pdf/1911.04136.pdf`.

Lobanov, S., Holtgrewe, N., Lin, J.F., Goncharov, A., 2017. Radiative conductivity and abundance of post-perovskite in the lowermost mantle. Earth and Planetary Science Letters 479, 43–49. doi:10.1016/j.epsl.2017.09.016.

Lobanov, S., Soubiran, F., Holtgrewe, N., Badro, J., Lin, J., Goncharov, A., 2019b. Opaque lowermost mantle URL: `https://arxiv.org/pdf/1909.01438.pdf`.

Manthilake, G.M., de Koker, N., Frost, D.J., McCammon, C.A., 2011. Lattice thermal conductivity of lower mantle minerals and heat flux from Earth's core. Proceedings of the National Academy of Sciences 108, 17901–17904. doi:10.1073/pnas.1110594108.

McWilliams, R.S., Konôpková, Z., Goncharov, A.F., 2015. A flash heating method for measuring thermal conductivity at high pressure and temperature: Application to Pt. Physics of the Earth and Planetary Interiors 247, 17–26. doi:10.1016/j.pepi.2015.06.002.

Mitrovica, J., Forte, A., 1997. Radial profile of mantle viscosity: Results from the joint inversion of convection and postglacial rebound observables. Journal of Geophysical Research: Solid Earth 102, 2751–2769. doi:10.1029/96JB03175.

Nakagawa, T., Tackley, P., 2014. Influence of combined primordial layering and recycled MORB on the coupled thermal evolution of Earth's mantle and core. Geochemistry, Geophysics, Geosystems 15, 619–633. doi:10.1002/2013GC005128.

Ohta, K., Yagi, T., Taketoshi, N., Hirose, K., Komabayashi, T., Baba, T., Ohishi, Y., Hernlund, J., 2012. Lattice thermal conductivity of $MgSiO_3$ perovskite and post-perovskite at the core–mantle boundary. Earth and Planetary Science Letters 349–350, 109–115. doi:10.1016/j.epsl.2012.06.043.

337 Okuda, Y., Ohta, K., Yagi, T., Sinmyo, R., Wakamatsu, T., Hirose, K., Ohishi, Y., 2017. The effect
338 of iron and aluminum incorporation on lattice thermal conductivity of bridgmanite at the Earth's
339 lower mantle. Earth and Planetary Science Letters 474, 25–31. doi:10.1016/j.epsl.2017.06.022.

340 Pozzo, M., Davies, C., Gubbins, D., Alfè, D., 2012. Thermal and electrical conductivity of iron at
341 Earth's core conditions. Nature 485, 355–358. doi:10.1038/nature11031.

342 Rainey, E.S.G., Kavner, A., 2014. Peak scaling method to measure temperatures in the laser-heated
343 diamond anvil cell and application to the thermal conductivity of MgO. Journal of Geophysical
344 Research: Solid Earth 119, 8154–8170. doi:10.1002/2014JB011267.

345 Ricolleau, A., Fei, Y., Cottrell, E., Watson, H., Deng, L., Zhang, L., Fiquet, G., Auzende, A.L.,
346 Roskosz, M., Morard, G., Prakapenka, V., 2009. Density profile of pyrolite under the lower mantle
347 conditions. Geophysical Research Letters 36, L06302. doi:10.1029/2008GL036759.

348 Ritsema, J., McNamara, A., Bull, A., 2007. Tomographic filtering of geodynamic models: implications
349 for model interpretation and large-scale mantle structure. Journal of Geophysical Research: Solid
350 Earth 112, B01303. doi:10.1029/2006JB004566.

351 Rudolph, M., Lekic, V., Lithgow-Bertelloni, C., 2015. Viscosity jump in Earth's mid-mantle. Science
352 350, 1349–1352. doi:10.1126/science.aad1929.

353 Stackhouse, S., Stixrude, L., Karki, B.B., 2015. First-principles calculations of the lattice ther-
354 mal conductivity of the lower mantle. Earth and Planetary Science Letters 427, 11–17.
355 doi:10.1016/j.epsl.2015.06.050.

356 Tang, X., Ntam, M.C., Dong, J., Rainey, E.S.G., Kavner, A., 2014. The thermal conductivity of
357 Earth's lower mantle. Geophysical Research Letters 41, 2746–2752. doi:10.1002/2014GL059385.

358 Yusenko, K.V., Khandarkhaeva, S., Fedotenko, T., Pakhomova, A., Gromilov, S.A., Dubrovinsky, L.,
359 Dubrovinskaia, N., 2019. Equations of state of rhodium, iridium and their alloys up to 70 GPa.
360 Journal of Alloys and Compounds 788, 212–218. doi:10.1016/j.jallcom.2019.02.206.

Supplemental Materials for "Thermal conductivity at the bottom of the Earth's lower mantle: measurements of pyrolite up to 120 GPa and 2500 K"

S1. Experimental Methods

Here we focus on details of the compression, heating, decompression, and thickness measurement procedure. Methods used to load samples are described in full detail in the main text. Details of laser-heating equipment, collection optics and the streak camera are described in McWilliams et al. (2015).

After loading each sample, pressure was increased to the desired value, which was measured using the diamond Raman edge pressure scale (Akahama and Kawamura, 2006). It was then left undisturbed for at least 30 minutes to allow the cell and gasket to relax. Pressure was measured again and thickness of insulation was measured using white-light interferometry assuming the refractive indices listed in Table 1. We first heated both iridium layers up to ∼2500 K for several minutes while adjusting laser alignment by small amounts, which serves two purposes: to convert the glass starting material to a polycrystalline assemblage of minerals (bridgmanite, ferropericlase, calcium-perovskite), and to align the continuous laser beams from left-side and right-side to each other and to the center of the area used for the spectroradiometric temperature measurement. Next, we stopped the continuous laser and started the second laser. In continuous mode, we align this laser beam to the same position by adjusting it until we generate thermal emissions at ∼1500 K at the same spot. For this laser, at least 100 times more power is directed to the left-side than to the right side of the sample, a ratio accomplished by tuning a half wave plate that is placed between two polarizing beam splitting cubes; see McWilliams et al. (2015) for details. This means the left-side is the "pulsed-side" in our setup, and the right side or "other-side" is not heated by the second laser. The precision of co-alignment is ± 1 μm for all five positions (laser 1 left, laser 1 right, laser 2 left, spectroradiometry left, spectroradiometry right) before and after the heating experiment. Such precision is evidenced by CCD images collected before, during, and after the experiment (e.g., Fig S1). Finally, we switch the second laser to pulsed mode.

To make the dynamic heating measurement we first use the mirror-configuration shown in Fig. S2a, in which thermal emissions from the pulsed-side are sent to the streak camera, and thermal emissions from the other-side are sent a CCD camera. We trigger a programmed sequence of events shown schematically in Fig. S2c. At time zero, the continuous laser turns on. One second later, a 1 kHz sequence of 8 μs square waves triggers the pulsed laser, resulting in ∼1 μs laser pulses. Simultaneously, the streak camera collects thermal emissions, repeating its sweep at 1 kHz frequency to build up signal. Five seconds later, the 1 kHz triggers stop and the streak camera is read out. One-hundred milliseconds later, the continuous laser stops. Sometime during the 5 s of data collection we collect a snapshot of thermal emissions from the right-side with exposure time ∼10 ms. We then switch to the mirror configuration of Fig. S2b in which the CCD camera views the pulsed-side and the streak camera views the other-side. We switch between mirror configurations at least two more times to ensure reproducibility of the temperature evolution. This is necessary since it is only currently possible to measure temperature versus time from one side with the one streak camera in our lab. The baseline

temperature typically drifts by 100 to 200 K between sets of 5 s experiments. If it drifts by more than 400 K, we tweak laser powers and try again. More crucial than the baseline temperature for determining k_{pyro} is the change in temperature above the baseline. For each data point presented here, the change in temperature was reproduced to within 10% at least once.

After several repetitions, we typically stopped heating, measured pressure and KCl or Ar thicknesses again, and decompressed to ambient pressure over ∼2 minutes. In the case of runs 4 and 5, we compressed beyond the pressure of the original data collection (62 or 124 GPa) and attempted to collect another data set (at 80 or 142 GPa). The data collection at 80 GPa was successful while the attempt at 142 GPa resulted in creation of a hole in the pulsed-side iridium layer. We then decompressed from 80 GPa or 142 GPa to ambient pressure. Next, we prepared the samples for electron microscopy using standard procedures. For the KCl loadings, we laser-drilled a circular cut with a diameter that is ∼80% of the culet diameter, and transferred the disc of rhenium plus sample chamber to carbon tape or a piece of polished Si. In the case of the Ar loading, the pressure medium evaporated upon decompression so we simply transferred the iridium-pyrolite-iridium sandwich to a piece of Si. We use silver epoxy to attach the recovered sample to the Si. We then cut cross sections using a focused ion beam. While cutting, we measure thickness of the recovered sample, a measurement that is crucial to determining thermal conductivity. After cutting the cross-sections we measure chemical composition using energy-dispersive spectroscopy (EDS) mapping (Fig. S3). We note that in a previous study by some of us, transmission-electron-microscopy measurements on recovered samples prepared using very similar sample synthesis methods to those used here, including the same starting glass, showed a polycrystalline assemblage of ferropericlase with molar ratio Fe/(Fe+Mg) = 0.17, bridgmanite with molar ratio Fe/(Fe+Mg) = 0.08, and calcium perovskite (Lobanov et al., 2019a). In this study, we measure the same bulk chemical composition as in (Lobanov et al., 2019a) and document chemical homogeneity across of the pyrolite sample when averaging over the ~ 1 μm spatial resolution of the EDS (top nine panels of Fig. S3). We also note sub-micron grains of a phase that is rich in heavy-elements in the electron backscatter image from the SEM (bottom panel of Fig. S3), which is consistent with the $\sim$ 100 to 400 nm grains of ferropericlase documented in STEM images of (Lobanov et al., 2019a) (their Fig. 1).

To determine thickness, d, we use thickness of the recovered samples as our primary source of information. We assume that the samples decompress elastically, following the equation of state of pyrolite, just as was assumed in Ohta et al. (2012), Imada et al. (2014), and Okuda et al. (2017) For the samples that were compressed after pulsed-heating measurements at 62 and 124 GPa, this only determines the thickness at the highest pressure achieved, i.e. 80 and 142 GPa. To interpolate to the lower pressures, we use a linear thinning approximation and add a 20% uncertainty to d_{pyro}. Specifically, we assume the samples reduced in thickness linearly as a function of pressure from their starting thicknesses of 4.73 and 5.97 μm to their thicknesses at the highest pressure they experienced, 1.07 and 1.8 μm, but admit that this interpolation adds an uncertainty of $\sim$ 20% to the total uncertainty of d_{pyro} (Table S1).

S2. Data analysis

S2.1. Data reduction

Raw data from the streak camera is reduced to normalized temperature versus time in five steps. First, geometric correction of the distorted streak image is accomplished by shifting measured intensity along lines of constant wavelength and interpolating to recreate an image on a Cartesian grid of pixels. The necessary shift is determined by calibration of the streak tube's distortion with a 1 MHz pulse-train of 1 ns-duration laser pulses from a supercontinuum laser. Second, the radiance correction is accomplished in the normal way by dividing all intensities of the two-dimensional image by intensity of a reference image from a tungsten lamp heated to 3187 K and multiplying by the theoretical radiance of the tungsten lamp at 3187 K. Third, we perform a two-parameter Planck function fit to the time-averaged intensity during a time interval in which total intensity varies relatively slowly (e.g., the shaded area in Fig. S4a). The two fitting parameters are temperature and emissivity. Examples of the fits for six streak camera images are shown in Fig. S4b. Fourth, we perform a one-parameter Planck function fit with emissivity fixed to the value determined in the first step, but now using narrow time intervals to determine temperature versus time. These time windows are 0.2 to 0.5 μs wide on a streak image of total duration 10 to 30 μs. Note that streak camera timing is calibrated from a sequence of 1 ns pulses at 1 MHz frequency from the supercontinuum laser. Time zero of the reduced data is defined arbitrarily, but is identical for the two streak camera images, from the pulsed side and the other side. Fig. S4d shows an example of the resulting temperature vs. time plots at 80 GPa, 2000 to 2500 K.

The fifth step of data reduction is to normalize changes in temperature. This step is not required, but it facilitates comparison of laboratory data collected with slightly different laser powers, alignment precisions, and sample positions. It also enables easier comparison of laboratory data to finite-element modeling results. We define normalized temperature from the pulsed heated side to be

$$\hat{T}_{\mathrm{pside}} = \frac{T - T_{0,\mathrm{pside}}}{\Delta T_{\mathrm{pside}}} \tag{S1}$$

and from the other side to be

$$\hat{T}_{\mathrm{oside}} = \frac{T - T_{0,\mathrm{oside}}}{\Delta T_{\mathrm{pside}}} \tag{S2}$$

where T is measured absolute temperature, $T_{0,\mathrm{pside}}$ and $T_{0,\mathrm{oside}}$ are the average temperatures measured before pulsed heating for the pulsed side and other side, and $\Delta T_{\mathrm{pside}}$ is the amplitude of the change in temperature of the pulsed side. Comparisons using this normalization scheme are useful because we model the heat equation as a linear differential equation with temperature-independent material properties. In reality, material properties are expected to vary by up to ∼20% over the temperature range probed in this experiment Stackhouse et al. (2015).

Fig. S5a shows that the data of Fig. S4 reduce to a single curve to within ∼10% when normalized by the measured value of $\Delta T_{\mathrm{pside}}$. Fig. S5b shows that the data are even more reproducible when $\Delta T_{\mathrm{pside}}$ is increased by 10% from the measured value for the 0.5 μs-resolution data to correct for the

blurring of intensity of thermal emissions over the time-axis of the streak camera. The 0.2 μs-resolution data is used in the fitting routines below. The 0.5 μs-resolution data is presented here in order to show a more complete picture of temperature evolution.

Spatially-resolved thermal emissions from the CCD image are reduced to temperature versus distance in a three step-process. First, we average over a short and wide region around the center of the hotspot to determine the measured intensity $I_{\text{meas}}(x)$. See example in Fig. S1. Second, we assume a Gaussian distribution of temperature

$$T(x) = (T_{\max} - 300)e^{-(x-x_0)/2\sigma^2} + 300 \tag{S3}$$

where $T_{\max}$ is the temperature measured on the streak camera prior to pulsed heating. We fit $I_{\text{meas}}(x)$ to the function

$$I(x) = I_{\text{dark}} + A \cdot P(T(x)) \tag{S4}$$

where I_{dark} is dark current of the CCD, A is a scaling factor, and P is the Planck function at 530 nm, the center of sensitivity of the green CCD pixels we use for measured intensity, I_{meas}.[1] In practice, this gives sufficient information for fitting our data to the finite element model. But to extract a more realistic the temperature distribution, we perform a third step of data reduction: "one-color" fits. We fix the values of I_{dark} and A to their values from the second step and fit for $T(x)$ at each distance, x, using the function same function as above, but no longer assume a Gaussian distribution of temperature.

S2.2. Finite element modeling

The following sections supplement the main text by detailing: (1) the implementation of the heat equation in method T and and method Q; (2) the procedure for determining the heating term in method Q; (3) the approximation of the modeled temperature; (4) assumptions for specific heat and density in the model; (5) uncertainties in model parameters; and (6) determination of uncertainties by searching parameter space for seventeen model parameters.

S2.3. Methods T and Q

The temperature in the experiment follows from the time-dependent heat diffusion equation with heat production. Analytical expressions of the solution of this equation in the complicated geometry explored in these experiments are not available, so we use finite element approximations to this equation using material properties and boundary conditions that closely mimic those of the experimental setup. The heat equation is

$$\rho c_v \frac{\partial T}{\partial t} - \nabla \cdot (k \nabla T) = Q. \tag{S5}$$

where ρ, c_v and k are the density, specific heat and thermal conductivity respectively. Q is the power deposited by an external heating source.

[1] https://www.flir.com/support-center/iis/machine-vision/application-note/understanding-color-interpolation/

The domain of interest is the sample chamber plus the nearby diamond and gasket. Assuming azimuthal symmetry, the computational domain is reduced to a two-dimensional cross section at uniform azimuth. The domain is meshed using `Gmsh` (Geuzaine and Remacle, 2009). An example of domain and mesh is shown in Fig. S6. The finite element approximation is computed using software based on the FEniCS project (Alnæs et al., 2015). The linear algebra systems are solved using MUMPS (Amestoy et al., 2000) via the PETSc library (Balay et al., 2019). Model errors due to discretization in space and time are less than 0.2% in normalized temperature, $\hat{T}$, or 2 K in absolute temperature. This is negligible compared to the $\sim$2% typical discrepancy between $\hat{T}$ of the best-fit model and its measured value.

A Dirichlet boundary condition of room temperature is enforced on the top, right and bottom exterior boundaries (i.e. at $z = \pm 40$ μm and $r = 100$ μm). A Neumann (symmetry) boundary condition is applied on the left exterior boundary (where $r = 0$).

In the case of method T, $Q = 0$, and a Dirichlet boundary condition is applied on the interior boundary between iridium and insulator at the pulsed side. This boundary condition enforces a time-dependent interpolation of experimentally measured temperature values. In the case of method Q, Q is estimated from the heat flux computation of a method T simulation, and no interior boundary condition is applied. Details are given in the following sections.

S2.4. $Q(t)$ in Method Q

The heating term for method Q is assumed to be non-zero only on the surfaces of the iridium and be dependent on space and time

$$Q(r,t) = Q_0(r)(1 + dQ(t)) \tag{S6}$$

with $dQ = 0$ on the non-pulsed side. The spatial components, $Q_0(r)$, are assumed to be Gaussians with the same width on both iridium surfaces. We determine the width and amplitudes of this Gaussian by fitting the pre-pulse temperature distributions to the measured temperature versus distance. The time-dependent function $dQ(t)$ is not known *a priori*, because the time-dependence was not measured accurately; the Newport 818-B8-40 25-MHz photodiode used to monitor laser pulse shape in this study output distorted waveforms, perhaps due to damage. Instead of relying on a measured laser-power, we use a bootstrap method to determine $dQ(t)$ in method Q. We start with the best fit to the data from method T and set $dQ(t)$ to the total flux out of the central disc of the coupler in method T, where the central disc extends from the coupler center to $r = 0.25$ μm in radius and across the full thickness of the iridium coating. Then, with one or two iterations of adding a broad Gaussian to the initial guess of dQ, followed by adjusting the fitted value of k_{pyro}, we converge to a fit with method Q that is as good as the fit with method T (e.g., Fig. S7). The small differences between the best-fit values of k_{pyro} between methods T and Q are listed in Table S1.

S2.5. An approximation of the modeled temperature

For convenience, we assume the measured temperature is the maximum temperature at the center of the hotspot, a simplification that makes no measurable difference for the model parameters studied

here. A more accurate approximation is to model the temperature that would be fit by spectroradiometry of thermal emissions averaged over all regions of the iridium surface that are measured in the streak camera (i.e. $r < 6.25$ μm). Fits with such a "Planck-averaged" model are compared to the more convenient "maximum-temperature" model in Fig. S8. The only model parameters that must be altered to create the same curves in the two models are the amplitudes of laser powers required to heat the sample to the measured temperature.

S2.6. Specific heat and density

To find a best fit of k_{pyro}, we must assume specific heat, c_v, and density, ρ, for all materials. Our assumption is that the pyrolite, iridium, and insulator all reach the Dulong-Petit limit for specific heat. For comparison, a Debye model at 2500 K for pyrolite with $\Theta_D = 1000$ K would predict specific heat 14% below the Dulong-Petit limit, which would propagate to a 5% reduction in k_{pyro}. This could be used as a correction to our fitted values of k_{pyro}, but the correction is uncertain and small compared to the 37% to 78% uncertainties reported here. The specific heat of iridium and the insulator have a smaller effect on the best fit value of k_{pyro}. We assume specific heat and density of gasket and diamond to be their values at ambient pressure and temperature. The sensitivity of best fit k_{pyro} to these assumptions is negligible (Fig. S9).

We assume density of pyrolite, iridium, and insulator that match the room temperature equations of state of these materials. This is an overestimate by a few percent that is nearly balanced by the underestimate that thicknesses of pyrolite, iridium, and insulator match their room temperature values. For example, volumetric thermal expansion at fixed pressure upon heating pyrolite from 300 to 2300 K at 80 GPa is ∼2%, causing a ∼2% decrease in density and if the expansion is isotropic, a ∼0.7% increase in sample thickness. Our uncertainty analysis shows that the former causes a ∼1% decrease in estimated value of thermal conductivity, while the latter causes a ∼1% increase in estimated value of thermal conductivity (Fig. S10 and Table S1). Equations of state are from Ricolleau et al. (2009) for pyrolite, from Yusenko et al. (2019) for iridium, from Dewaele et al. (2012) for KCl, and from Errandonea et al. (2006) for Ar.

S2.7. Uncertainty in model parameters

'Method T' involves twenty-four parameters in total. Specific heat and density always appear together in the heat equation as $c_v\rho$, reducing the number of parameters to nineteen.

Nine parameters that have negligible effect on the best-fit k_{pyro} are d_{diamond}, $d_{\mathrm{ins,pside}}$, k_{diamond}, k_{Re}, r_{diamond}, r_{ins}, r_{pyro}, $c_v\rho_{\mathrm{Re}}$, $c_v\rho_{\mathrm{diamond}}$, where d is thickness, r is radius and $c_v\rho$ is the product of specific heat and density. The first seven are shown to have negligible effect on the best-fit at 80 GPa in Fig. S9. It is intuitive that the final two have negligible effect; $c_v\rho$ of diamond and rhenium vary much less than thermal conductivity with pressure and temperature, and even thermal conductivity of diamond and rhenium have negligible effect.

Uncertainties due to seven of the ten remaining parameters are listed in Table S1. These are four geometric parameters, d_{pyro}, d_{Ir}, $d_{\mathrm{ins,oside}}$, T_{FWHM}, and three values of $c_v\rho$ for pyrolite, iridium and insulator. For convenience, we refer to uncertainties in $c_v\rho$ as 'σ_c', which we assume to be 20%. To

enable wide searches of parameter space, we vary parameters by even units in log-space and keep track of all uncertainties in log space. For example, these 20% uncertainties are represented in Table S1 as $\sigma_{\log c} = \log_{10}(1.2) = 0.079$. The uncertainties in geometric parameters are from the irregularity of thicknesses and the slight differences in T_{FWHM} measured from pulsed side and other side.

The three remaining parameters are the free parameters, k_{pyro}, k_{Ir}, k_{ins}.

S2.8. Propagation of uncertainties

First, we determine a confidence interval around the best fit value of k_{pyro}, allowing k_{ins} and k_{coupler} to vary along with k_{sam} but keeping all other parameters fixed. To determine the confidence interval, we first perform a grid search in three-dimensional parameter space:

$$\log\mathbf{k} = (\log k_{\mathrm{pyro}}, \log k_{\mathrm{ins}}, \log k_{\mathrm{coupler}}) \tag{S7}$$

Then we find the contour of RMS (root mean square deviation of model to measurement) that is $\sqrt{2}$-times the minimum RMS. An example is the darkest blue contour in Fig. S11. Projections onto one-dimension in parameter-space are shown in Fig. S12. The maximum and minimum of $\log k_{\mathrm{pyro}}$ of this contour is the confidence interval and we denote the positive and negative deviations from best fit value of $\log k_{\mathrm{pyro}}$ as $\sigma^{\pm}_{\log k_{\mathrm{pyro}},\mathbf{k}}$. We note that the limit of $\sqrt{2}$ is a conservative estimate of the 1σ confidence interval, because in general the 1σ confidence interval is defined where $\mathrm{RMS} = \sqrt{\mathrm{RMS}^2_{\mathrm{min}}(1 + \frac{1}{n^2})}$ where n is the number of independent measurements in the fitted data (i.e. temperatures at different times). In practice, we do not know the exact value of n, so we set $n = 1$, the most conservative value. To visualize the contour, we first project onto the $k_{\mathrm{pyro}} - k_{\mathrm{ins}}$ plane by taking the minimum RMS over all values of k_{coupler}, and then plot contours with the "Axes.tricontour" function within Python's matplotlib library.

Note that for practical reasons, we have restricted our search to $k_{\mathrm{coupler}} > 30$ W/m/K, a conservative lower bound given that the ambient pressure value of k_{Ir} is 100 to 120 W/m/K at 1000 to 2000°C (Cagran and Pottlacher (2007) and www.pgmdatabase.com) and we expect a positive pressure dependence of ∼1% per GPa as measured for Pt (McWilliams et al., 2015). Even if k_{Ir} were less than 30 W/m/K, the resulting best fit would likely have a higher k_{ins} to compensate for the low k_{Ir} and no change in k_{ins}, as is seen in Fig. S11.

Second, we propagate errors from uncertainties in measured and assumed parameters. We assume the uncertainty on each parameter is independent from the uncertainty on all parameters except for k_{pyro}, allowing us to independently co-vary each of twelve parameters with k_{pyro} to determine how errors propagate. We perform a grid search in fourteen sets of a two-dimensional parameter space and visualize the result by contours of RMS in Figs. S10 and S9. More important than the RMS contours for our error analysis, though, are the slopes $\Delta\log k^*_{\mathrm{pyro}}/\Delta\log p$ where the star denotes the best fit and p is one of the twelve parameters. These slopes are also plotted in each panel of Figs. S10 and S9. Note that all slopes in Fig. S9 are zero, which is why these seven parameters are not included in the uncertainty estimation of Table S1. The contribution of each parameter's uncertainty to the

uncertainty of $\log k_{\rm pyro}$ is

$$\sigma_{\log k_{\rm pyro},p} = \frac{\Delta \log k^*_{\rm pyro}}{\Delta \log p} \sigma_{\log p} \tag{S8}$$

where σ_p is the uncertainty in parameter p.

To combine propagated uncertainties with the confidence interval determined in our search of $(k_{\rm pyro}, k_{\rm coupler}, k_{\rm ins})$ space, we add in quadrature, since we assume independence of uncertainties:

$$\sigma^{\pm}_{\log k_{\rm pyro}} = \sqrt{(\sigma^{\pm}_{\log k_{\rm pyro},\mathbf{k}})^2 + \Sigma_p (\sigma_{\log k_{\rm pyro},p})^2} \tag{S9}$$

References

Akahama, Y., Kawamura, H., 2006. Pressure calibration of diamond anvil Raman gauge to 310 GPa. J. Appl. Phys. 100, 043516. doi:10.1063/1.2335683.

Alnæs, M.S., Blechta, J., Hake, J., Johansson, A., Kehlet, B., Logg, A., Richardson, C., Ring, J., Rognes, M.E., Wells, G.N., 2015. The FEniCS Project Version 1.5. Archive of Numerical Software 3, 9–23. doi:10.11588/ans.2015.100.20553.

Amestoy, P.R., Duff, I.S., L'Excellent, J.Y., 2000. Multifrontal parallel distributed symmetric and unsymmetric solvers. Computer Methods in Applied and Mechanical Engineering 184, 501–520. doi:10.1016/S0045-7825(99)00242-X.

Ammann, M.W., Walker, A.M., Stackhouse, S., Wookey, J., Forte, A.M., Brodholt, J.P., Dobson, D.P., 2014. Variation of thermal conductivity and heat flux at the Earth's core mantle boundary. Earth and Planetary Science Letters 390, 175–185. doi:10.1016/j.epsl.2014.01.009.

Balay, S., Abhyankar, S., Adams, M.F., Brown, J., Brune, P., Buschelman, K., Dalcin, L., Eijkhout, V., Gropp, W.D., Kaushik, D., Knepley, M.G., May, D.A., McInnes, L.C., Mills, R.T., Munson, T., Rupp, K., Sanan, P., Smith, B.F., Zampini, S., Zhang, H., Zhang, H., 2019. PETSc Web page. URL: `http://www.mcs.anl.gov/petsc`.

Brown, J.M., Shankland, T.J., 1981. Thermodynamic parameters in the Earth as determined from seismic profiles. Geophysical Journal International 66, 579–596. doi:10.1111/j.1365-246X.1981.tb04891.x.

Cagran, C., Pottlacher, G., 2007. Thermophysical properties and normal spectral emittance of iridium up to 3500 K. International Journal of Thermophysics 28, 697–710. doi:10.1007/s10765-007-0188-9.

Chen, B., Gleason, A.E., Yan, J.Y., Koski, K.J., Clark, S., Jeanloz, R., 2010. Elasticity, strength, and refractive index of argon at high pressures. Physical Review B 81, 144110. doi:10.1103/PhysRevB.81.144110.

Dalton, D.A., Hsieh, W.P., Hohensee, G.T., Cahill, D.G., Goncharov, A.F., 2013. Effect of mass disorder on the lattice thermal conductivity of MgO periclase under pressure. Scientific Reports 3, 2400. doi:10.1038/srep02400.

Dekura, H., Tsuchiya, T., Tsuchiya, J., 2013. Ab initio lattice thermal conductivity of $MgSiO_3$ perovskite as found in Earth's lower mantle. Physical Review Letters 110, 025904. doi:10.1103/PhysRevLett.110.025904.

Dewaele, A., Belonoshko, A.B., Garbarino, G., Occelli, F., Bouvier, P., Hanfland, M., Mezouar, M., 2012. High-pressure-high-temperature equation of state of KCl and KBr. Physical Review B 85, 214105. doi:10.1103/PhysRevB.85.214105.

Errandonea, D., Boehler, R., Japel, S., Mezouar, M., Benedetti, L.R., 2006. Structural transformation of compressed solid Ar: An x-ray diffraction study to 114 GPa. Physical Review B 73, 092106. doi:10.1103/PhysRevB.73.092106.

Geuzaine, C., Remacle, J.F., 2009. Gmsh: A 3-D finite element mesh generator with built-in pre- and post-processing facilities. International Journal for Numerical Methods in Engineering 79, 1309–1331. doi:doi.org/10.1002/nme.2579.

Ghaderi, N., Zhang, D.B., Zhang, H., Xian, J., Wentzcovitch, R.M., Sun, T., 2017. Lattice thermal conductivity of $MgSiO_3$ perovskite from first principles. Scientific Reports 7, 5417. doi:10.1038/s41598-017-05523-6.

Goncharov, A.F., Beck, P., Struzhkin, V.V., Haugen, B.D., Jacobsen, S.D., 2009. Thermal conductivity of lower-mantle minerals. Physics of the Earth and Planetary Interiors 174, 24–32. doi:10.1016/j.pepi.2008.07.033.

Goncharov, A.F., Lobanov, S.S., Tan, X., Hohensee, G.T., Cahill, D.G., Lin, J.F., Thomas, S.M., Okuchi, T., Tomioka, N., 2015. Experimental study of thermal conductivity at high pressures: Implications for the deep Earth's interior. Physics of the Earth and Planetary Interiors 247, 11–16. doi:10.1016/j.pepi.2015.02.004.

Haigis, V., Salanne, M., Jahn, S., 2012. Thermal conductivity of MgO, $MgSiO_3$ perovskite and post-perovskite in the Earth's deep mantle. Earth and Planetary Science Letters 355–356, 102 – 108. doi:10.1016/j.epsl.2012.09.002.

Hsieh, W.P., Deschamps, F., Okuchi, T., Lin, J.F., 2017. Reduced lattice thermal conductivity of Fe-bearing bridgmanite in earth's deep mantle. Journal of Geophysical Research: Solid Earth 122, 4900–4917. doi:10.1002/2017JB014339.

Hsieh, W.P., Deschamps, F., Okuchi, T., Lin, J.F., 2018. Effects of iron on the lattice thermal conductivity of Earth's deep mantle and implications for mantle dynamics. Proceedings of the National Academy of Sciences 115, 4099–4104. doi:10.1073/pnas.1718557115.

Imada, S., Ohta, K., Yagi, T., Hirose, K., Yoshida, H., Nagahara, H., 2014. Measurements of lattice thermal conductivity of MgO to core-mantle boundary pressures. Geophysical Research Letters 41, 4542–4547. doi:10.1002/2014GL060423.

Jones, T., Maguire, R., van Keken, P., Ritsema, J., in revision. Subducted oceanic crust as the origin of lower-mantle structures. Progress in the Earth and Planetary Sciences .

Katsura, T., Yoneda, A., Yamazaki, D., Yoshino, T., Ito, E., 2010. Adiabatic temperature profile in the mantle. Physics of the Earth and Planetary Interiors 183, 212 – 218. doi:10.1016/j.pepi.2010.07.001. special Issue on Deep Slab and Mantle Dynamics.

Konôpková, Z., McWilliams, R.S., Gómez-Pérez, N., Goncharov, A.F., 2016. Direct measurement of thermal conductivity in solid iron at planetary core conditions. Nature 534, 99–101. doi:10.1038/nature18009.

Lau, H., Mitrovica, J., Austermann, J., Crawford, O., Al-Attar, D., Latychev, K., 2016. Inferences of mantle viscosity based on ice age data sets: Radial structure. Journal of Geophysical Research: Solid Earth 121, 6991–7012. doi:10.1002/2016JB013043.

Lobanov, S., Holtgrewe, N., Ito, G., Badro, J., Piet, H., Nabiei, F., Lin, J., Bayarjargal, L., Wirth, R., Schriber, A., Goncharov, A., 2019a. Blocked radiative heat transport in the hot pyrolitic lower mantle URL: `https://arxiv.org/pdf/1911.04136.pdf`.

Lobanov, S., Holtgrewe, N., Lin, J.F., Goncharov, A., 2017. Radiative conductivity and abundance of post-perovskite in the lowermost mantle. Earth and Planetary Science Letters 479, 43–49. doi:10.1016/j.epsl.2017.09.016.

Lobanov, S., Soubiran, F., Holtgrewe, N., Badro, J., Lin, J., Goncharov, A., 2019b. Opaque lowermost mantle URL: `https://arxiv.org/pdf/1909.01438.pdf`.

Manthilake, G.M., de Koker, N., Frost, D.J., McCammon, C.A., 2011. Lattice thermal conductivity of lower mantle minerals and heat flux from Earth's core. Proceedings of the National Academy of Sciences 108, 17901–17904. doi:10.1073/pnas.1110594108.

McWilliams, R.S., Konôpková, Z., Goncharov, A.F., 2015. A flash heating method for measuring thermal conductivity at high pressure and temperature: Application to Pt. Physics of the Earth and Planetary Interiors 247, 17–26. doi:10.1016/j.pepi.2015.06.002.

Mitrovica, J., Forte, A., 1997. Radial profile of mantle viscosity: Results from the joint inversion of convection and postglacial rebound observables. Journal of Geophysical Research: Solid Earth 102, 2751–2769. doi:10.1029/96JB03175.

Nakagawa, T., Tackley, P., 2014. Influence of combined primordial layering and recycled MORB on the coupled thermal evolution of Earth's mantle and core. Geochemistry, Geophysics, Geosystems 15, 619–633. doi:10.1002/2013GC005128.

716 Ohta, K., Yagi, T., Taketoshi, N., Hirose, K., Komabayashi, T., Baba, T., Ohishi, Y., Hernlund, J.,
717 2012. Lattice thermal conductivity of $MgSiO_3$ perovskite and post-perovskite at the core–mantle
718 boundary. Earth and Planetary Science Letters 349–350, 109–115. doi:10.1016/j.epsl.2012.06.043.

719 Okuda, Y., Ohta, K., Yagi, T., Sinmyo, R., Wakamatsu, T., Hirose, K., Ohishi, Y., 2017. The effect
720 of iron and aluminum incorporation on lattice thermal conductivity of bridgmanite at the Earth's
721 lower mantle. Earth and Planetary Science Letters 474, 25–31. doi:10.1016/j.epsl.2017.06.022.

722 Pozzo, M., Davies, C., Gubbins, D., Alfè, D., 2012. Thermal and electrical conductivity of iron at
723 Earth's core conditions. Nature 485, 355–358. doi:10.1038/nature11031.

724 Rainey, E.S.G., Kavner, A., 2014. Peak scaling method to measure temperatures in the laser-heated
725 diamond anvil cell and application to the thermal conductivity of MgO. Journal of Geophysical
726 Research: Solid Earth 119, 8154–8170. doi:10.1002/2014JB011267.

727 Ricolleau, A., Fei, Y., Cottrell, E., Watson, H., Deng, L., Zhang, L., Fiquet, G., Auzende, A.L.,
728 Roskosz, M., Morard, G., Prakapenka, V., 2009. Density profile of pyrolite under the lower mantle
729 conditions. Geophysical Research Letters 36, L06302. doi:10.1029/2008GL036759.

730 Ritsema, J., McNamara, A., Bull, A., 2007. Tomographic filtering of geodynamic models: implications
731 for model interpretation and large-scale mantle structure. Journal of Geophysical Research: Solid
732 Earth 112, B01303. doi:10.1029/2006JB004566.

733 Rudolph, M., Lekic, V., Lithgow-Bertelloni, C., 2015. Viscosity jump in Earth's mid-mantle. Science
734 350, 1349–1352. doi:10.1126/science.aad1929.

735 Stackhouse, S., Stixrude, L., Karki, B.B., 2015. First-principles calculations of the lattice ther-
736 mal conductivity of the lower mantle. Earth and Planetary Science Letters 427, 11–17.
737 doi:10.1016/j.epsl.2015.06.050.

738 Tang, X., Ntam, M.C., Dong, J., Rainey, E.S.G., Kavner, A., 2014. The thermal conductivity of
739 Earth's lower mantle. Geophysical Research Letters 41, 2746–2752. doi:10.1002/2014GL059385.

740 Yusenko, K.V., Khandarkhaeva, S., Fedotenko, T., Pakhomova, A., Gromilov, S.A., Dubrovinsky, L.,
741 Dubrovinskaia, N., 2019. Equations of state of rhodium, iridium and their alloys up to 70 GPa.
742 Journal of Alloys and Compounds 788, 212–218. doi:10.1016/j.jallcom.2019.02.206.

P (GPa)	$\sigma_{\log(p)}$ d_{pyro}	$C_{v,\text{pyro}}$	$C_{v,\text{coupler}}$	$C_{v,\text{ins}}$	d_{coupler}	$\text{d}_{\text{ins,oside}}$	T_{FWHM}
40	0.079	0.079	0.079	0.079	0.146	0.041	0.079
41	0.079	0.079	0.079	0.079	0.146	0.041	0.079
62	0.146	0.079	0.079	0.079	0.204	0.041	0.079
68	0.114	0.079	0.079	0.079	0.176	0.041	0.079
80	0.079	0.079	0.079	0.146	0.079	0.079	0.041
124	0.146	0.079	0.079	0.079	0.204	0.146	0.079
	$\sigma_{\log(k_{\text{pyro}}),p}$ d_{pyro}	$C_{v,\text{pyro}}$	$C_{v,\text{coupler}}$	$C_{v,\text{ins}}$	d_{coupler}	$\text{d}_{\text{ins,oside}}$	T_{FWHM}
40	0.111	0.031	0.002	0.01	0.029	0	-0.05
41	0.117	0.039	0.001	0.013	0.016	0	-0.04
62	0.194	0.022	0.001	0.01	0.03	-0.002	-0.045
68	0.152	0.02	0.001	0.02	0.013	-0.001	-0.02
80	0.108	0.029	0.014	0.021	-0.037	0.001	-0.001
124	0.205	0.025	0.001	0.007	0.027	-0.034	-0.039
	$\sigma^{+}_{\log(k_{\text{pyro}}),\mathbf{k}}$	$\sigma^{-}_{\log(k_{\text{pyro}}),\mathbf{k}}$	$\sigma^{+}_{\log(k_{\text{pyro}})}$	$\sigma^{-}_{\log(k_{\text{pyro}})}$	Method T $\log(k)$	Method Q $\log(k_{\text{pyro}})$	Method Q-T $\Delta\log(k_{\text{pyro}})$
40	0.046	0.044	0.137	0.137	0.602	0.699	0.097
41	0.103	0.161	0.167	0.208	0.771	0.785	0.014
62	0.073	0.07	0.216	0.215	0.672	0.663	-0.009
68	0.098	0.082	0.184	0.176	0.58	0.633	0.054
80	0.064	0.08	0.136	0.144	0.58	0.591	0.011
124	0.067	0.039	0.225	0.218	0.756	0.771	0.015

Table S1: Error analysis. Top third: uncertainties, $\sigma_{\log(p)}$, for all input parameters, p. Middle third: propagation of $\sigma_{\log(p)}$ to uncertainty in $\log(k_{\text{pyro}})$. Bottom third: The first two columns list the uncertainties derived from searching through the free parameter space, $\mathbf{k}$ =(k_{pyro},k_{ins},k_{Ir}). The third and fourth columns list the quadrature sum of the first two columns with the $\sigma_{\log(k_{\text{pyro}})}$. The final three columns list best fit values of $\log(k_{\text{pyro}})$ from method T and method Q, as well as the the difference thereof.

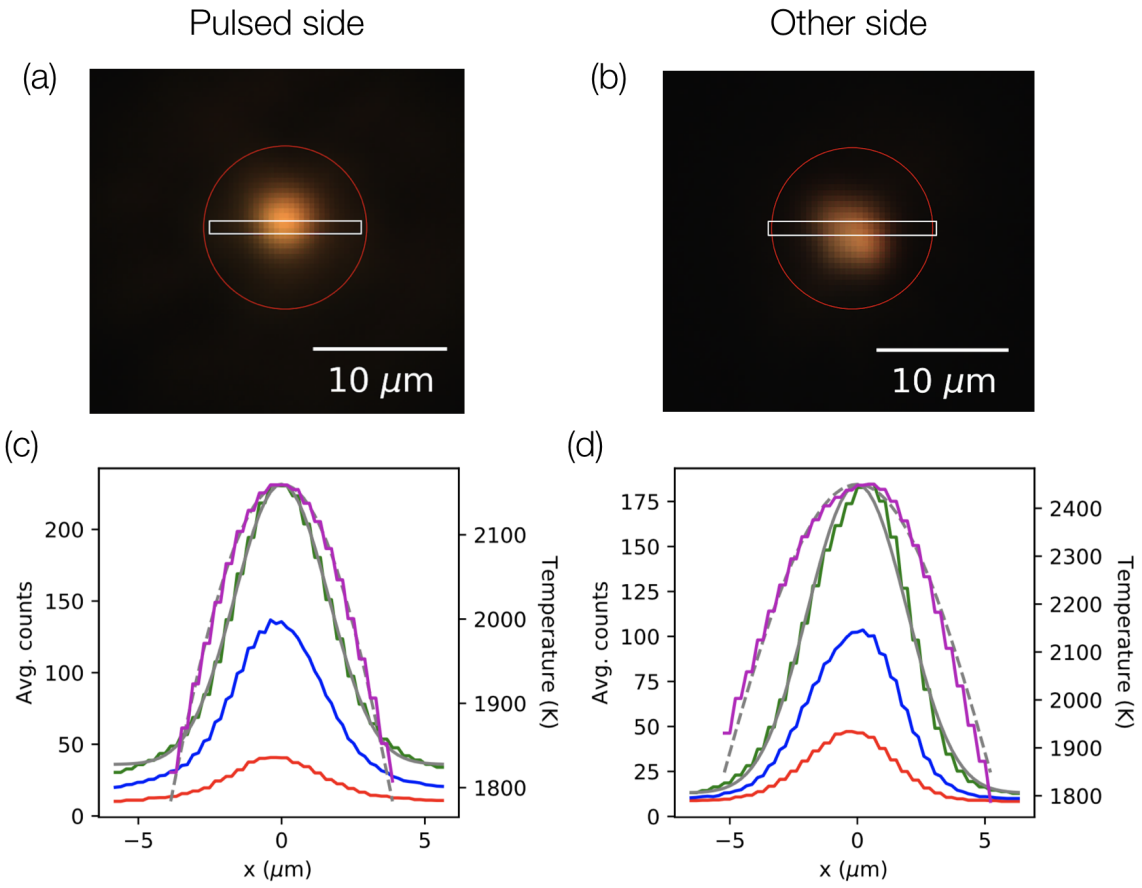

Figure S1: Spatial distribution of thermal emissions and temperature at 80 GPa. (a,b) CCD images collected during the thermal conductivity measurements using a 10 ms exposure time. Red circle outlines the region from which light is collected on the streak camera. White rectangle outlines the region used for the line-outs in (c,d). (c,d) Red, green, and blue curves show the spatial distribution of the hotspot intensity as measured in the three color channels of the CCD camera, averaged over the height of the white rectangles in (a,b). The CCD color channels have maximum sensitivity at 640 nm for red, 530 nm for green, and 470 nm for blue, each with ~ 50 nm FWHM. Grey solid line shows the fit to the green data of the function $I(x) = I_{\mathrm{dark}} + A \cdot P(T(x))$ for the Gaussian distribution, $T(x)$, described in equation S3. Grey dashed line shows $T(x)$. Purple shows $T(x)$ with the Gaussian assumption lifted but I_{dark} and A fixed to their values from the grey fit.

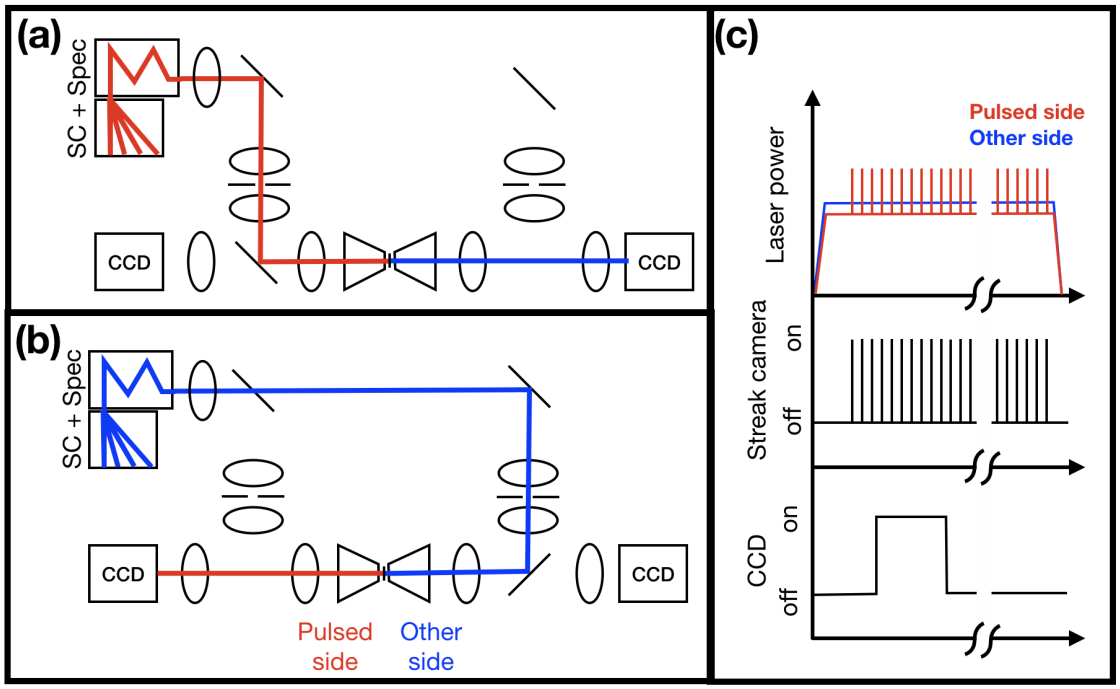

Figure S2: (a,b) Schematic of optics for collection of thermal emissions from (a) pulsed side and (b) other side. Ovals represent lenses, angled line represent mirrors, broken horizontal lines represent pinholes, trapezoids represent diamond anvils, "SC" labels the streak camera, and "Spec" labels the spectrometer. (c) Schematic of timing of laser power, streak camera exposure, and CCD camera exposure. Colored lines shows the path of light emitted from the two sides of the sample in (a,b) and of the laser power incident on the sample from the two sides in (c). Red lines represent the pulsed side and blue lines represent the other side.

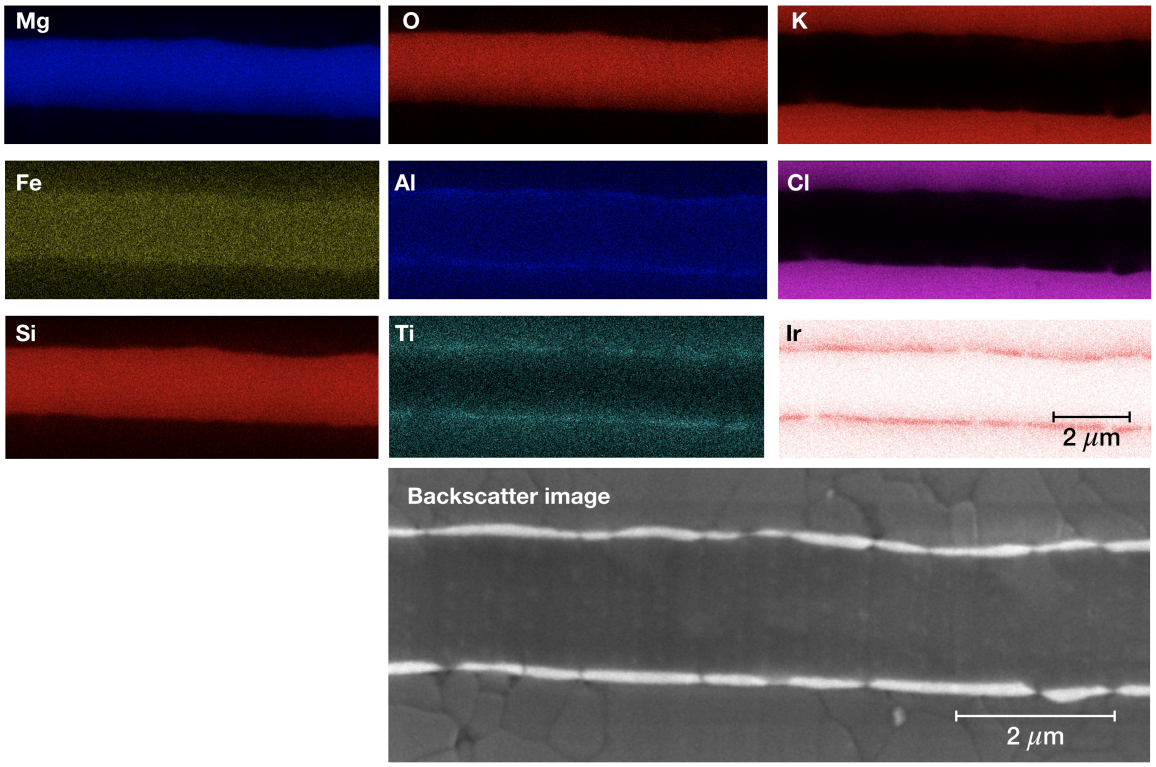

Figure S3: Elemental maps of sample recovered from run 4 (decompressed from 80 GPa), along with SEM backscatter image of the same region.

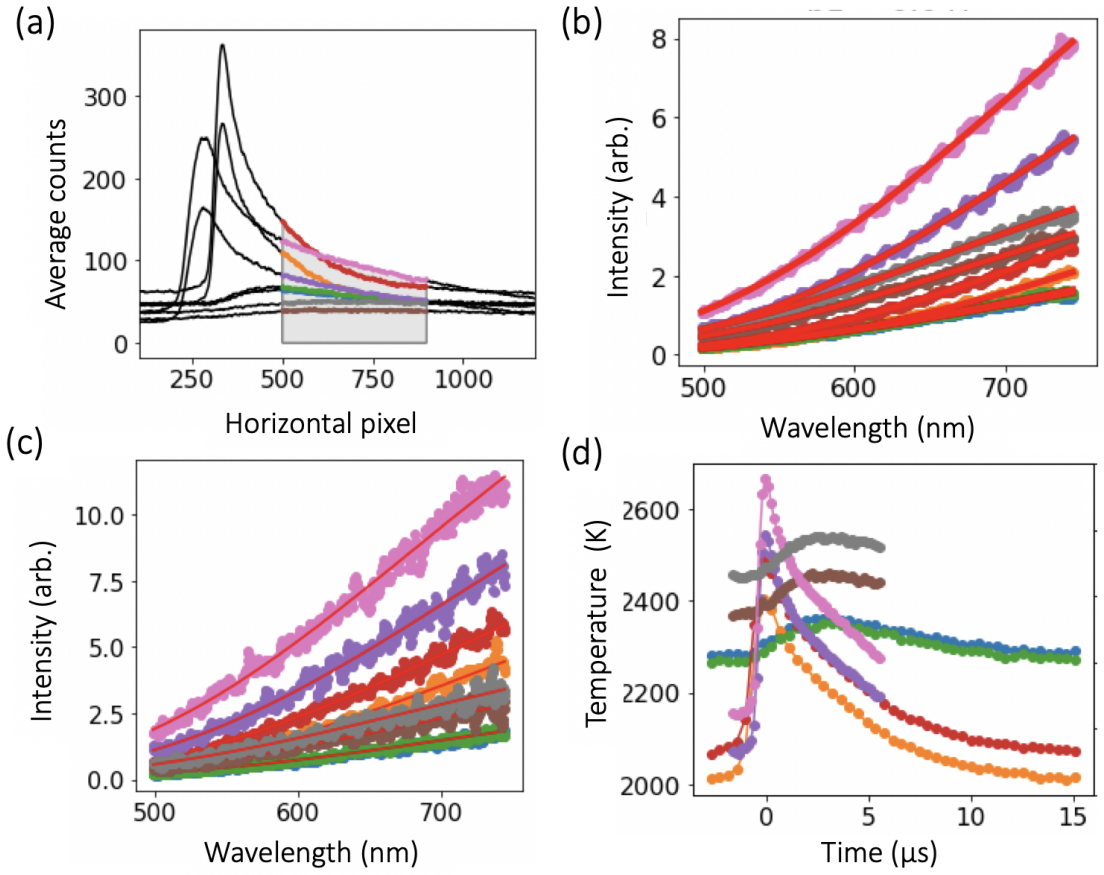

Figure S4: Data processing steps used to determine temperature versus time for the 80 GPa data set. (a) Average number of counts as a function of the horizontal pixel of the streak camera image. Eight traces are shown in black with colored overlay: four traces at 10 μs streak duration (pink, purple for pulsed side; brown, grey for other side), four at 30 μs streak duration (red, orange for pulsed side; blue, green for other side). The shaded region from 500 to 900 pixels shows the region used to generate (b). (b) Corrected intensity in the grey region of (a) versus wavelength. The correction is accomplished in the normal way for spectroradiometry: by calibrating the system response with a tungsten lamp of known temperature. Red curves are two-parameter Planck fits. (c) Examples of corrected intensity of a narrow time window versus wavelength. The time windows chosen for this plot are 0.2 to 0.5 μs wide, centered on the streak image (i.e. horizontal pixel # 600). Red curves are one parameter Planck fits, assuming the value of emissivity fitted in (b). (d) Temperature versus time for all six traces. Temperatures at each time are fitted as shown in (c).

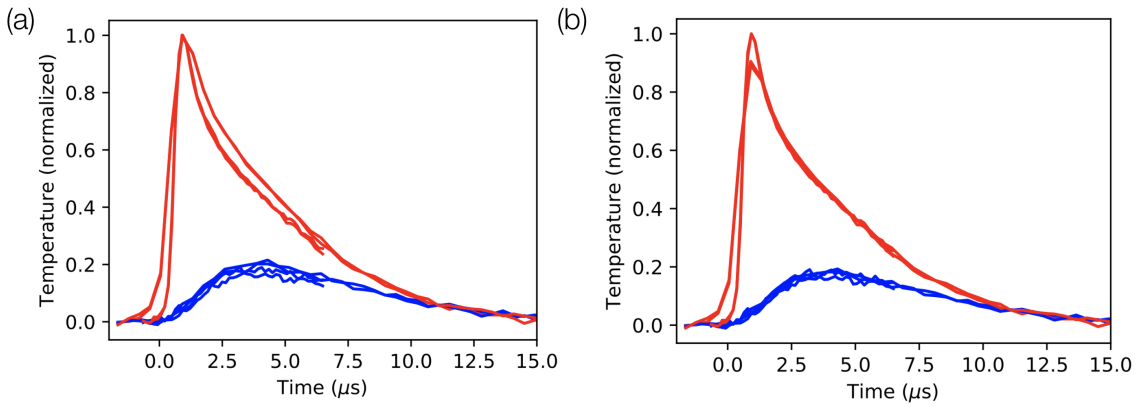

Figure S5: Normalized temperature-time curves from data at 80 GPa. The eight data sets of Fig. S4 are overlaid in each plot, with data from the pulsed side in red and from the other side in blue. (a) Automated normalization. (b) By hand normalization of 30 μs data set, automated normalization of 10 μs data set. By hand, we choose normalization factors to make all data sets overlap at all times when temperature changes relatively slowly.

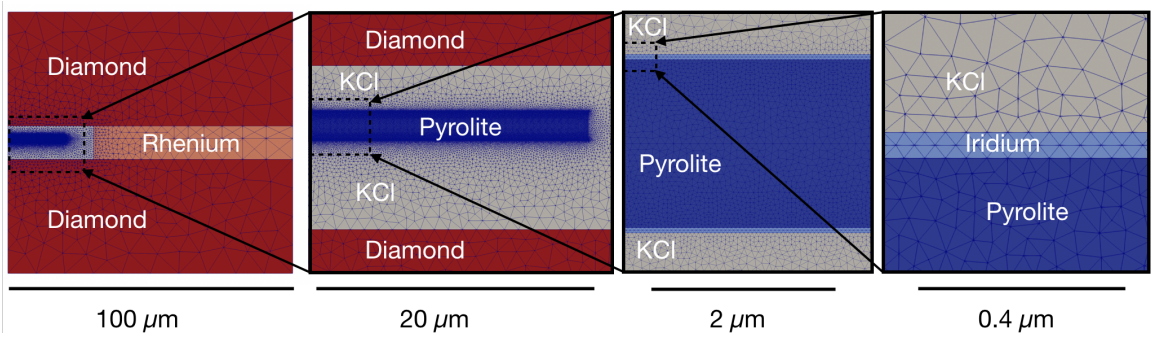

Figure S6: Mesh used to simulate the heating experiment at 80 GPa.

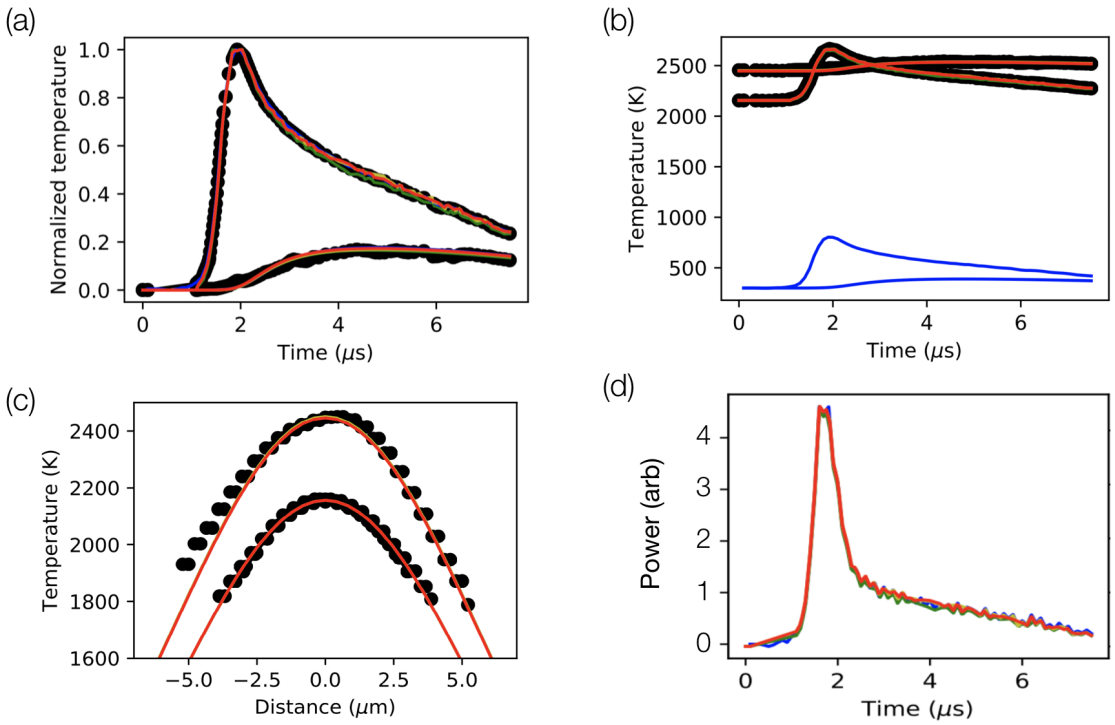

Figure S7: Comparison of method T and method Q. Data (black points), method T simulation (blue), method Q simulation with heating term $dQ = dQ_T$ inferred from the method T result (green), method Q simulation with $dQ = dQ_T + G$ where G is a Gaussian of 0.08 amplitude relative to dQ_T centered at $t = 6$ μs with 6 μs FWHM (yellow), method Q simulation with $dQ = dQ_T + G$ and k_{sam} increased by 3% to 3.9 W/m/K. (red)

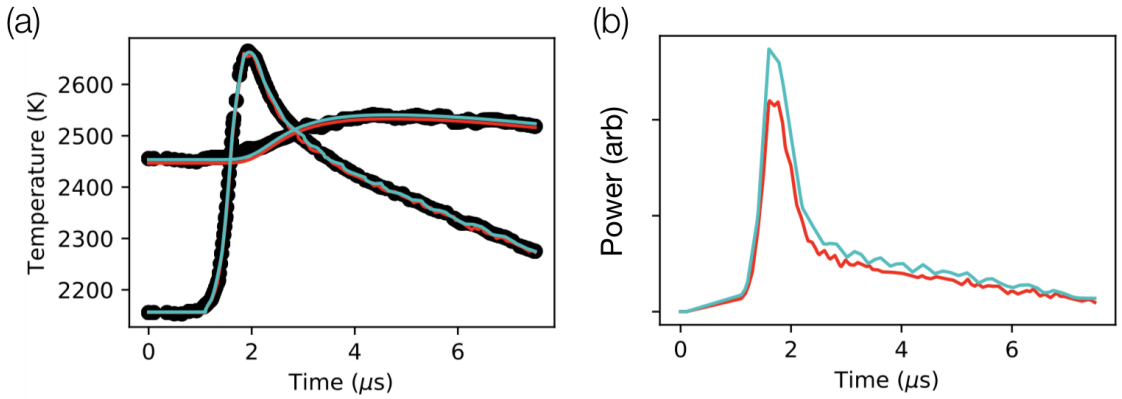

Figure S8: Comparison of method T with the "maximum-temperature" approximation (red) and the "Planck-averaged temperature" model (cyan). The Planck-averaged temperatures require 25% higher laser powers, as shown in (b), but all other model parameters are identical.

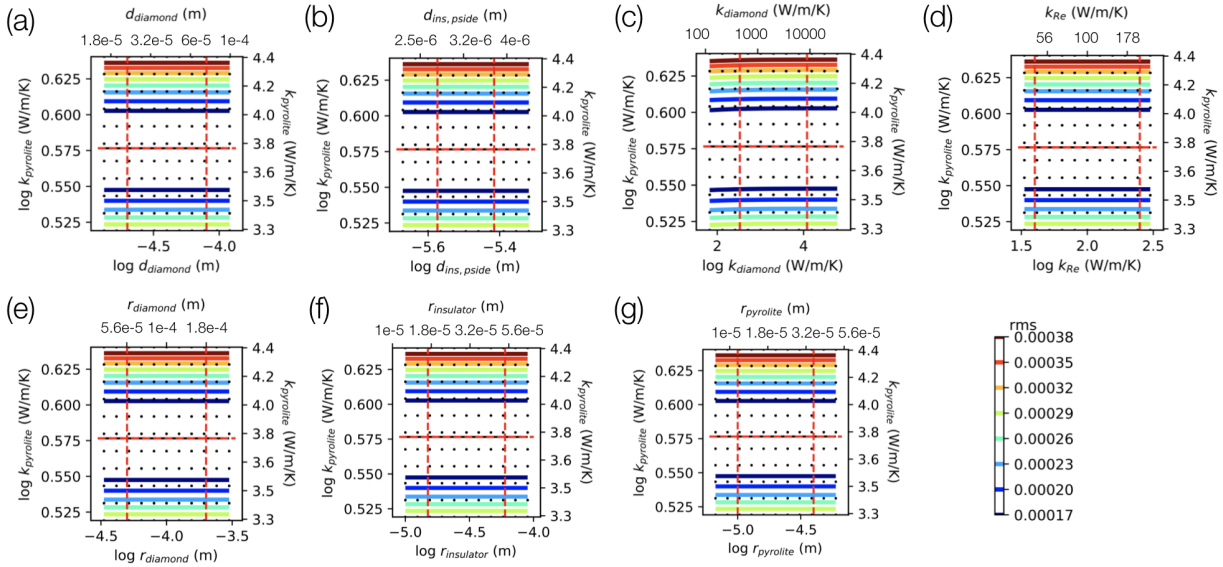

Figure S9: Rainbow-colored contours show RMS deviations of model to measured temperatures in the space $k_{\rm pyro} - p$ where the parameter p is labeled on the x-axis. The seven parameters plotted here have uncertainties that propagate to negligible uncertainty in $k_{\rm pyro}$. The black dashed line shows the linear fit of the best fit $k^*_{\rm pyro}(p)$ versus p. Vertical red dashed lines show the range of possible values of p, while horizontal red dashed lines show the propagation of this range onto the best fit $k_{\rm pyro}$. Black dots mark the parameters values that were simulated.

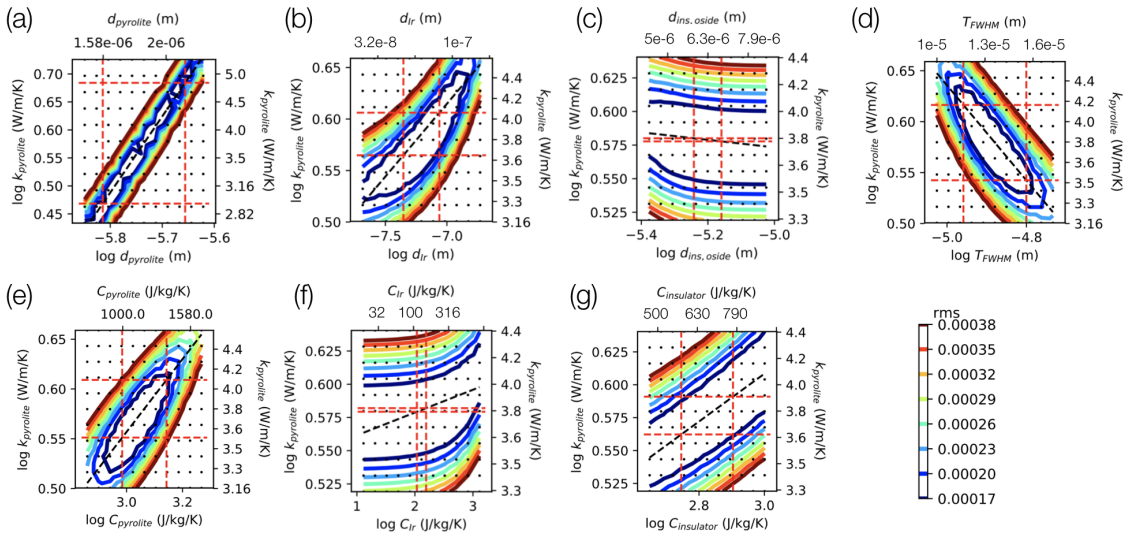

Figure S10: Same as Fig. S9, but for seven parameters, p, whose uncertainties propagate to uncertainties in $k_{\rm pyro}$ that we tabulate in Table S1

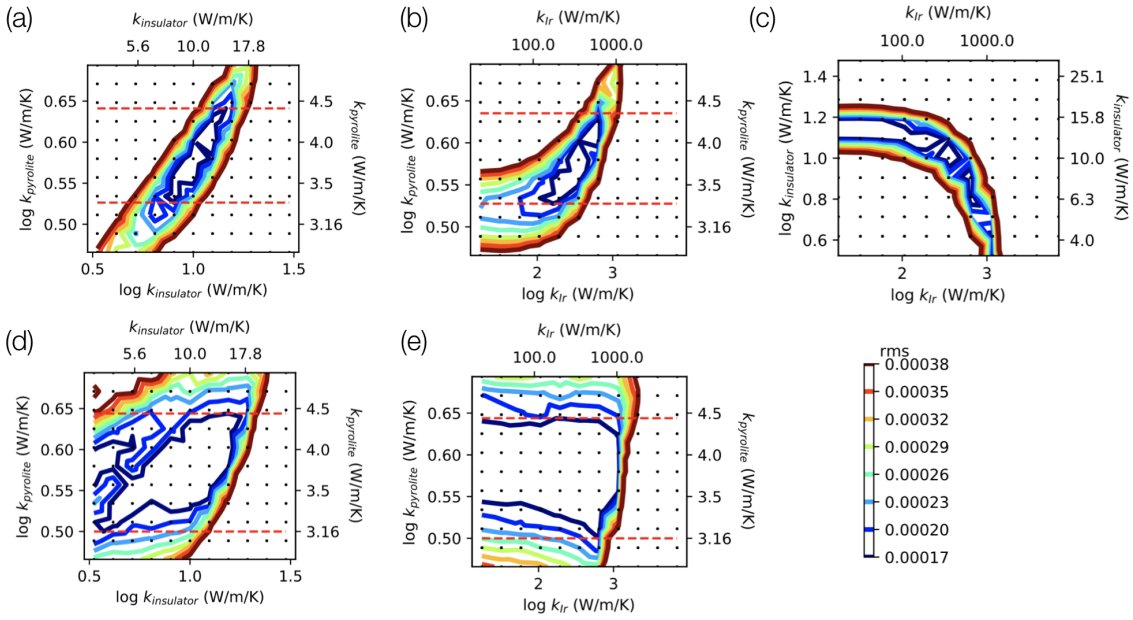

Figure S11: Contours of RMS deviation of fits to data at 80 GPa. (a,b,c) Two-dimensional cross sections of contours in the three-dimensional free parameter space, $\mathbf{k} = (k_{\text{pyro}}, k_{\text{ins}}, k_{\text{coupler}})$. (d-e) Contours of RMS minimized over the parameter not plotted. I.e., (d) shows contours of minima over all k_{Ir} , while (e) shows contours of minima over all k_{ins}. Red dashed lines mark the minimum contour, RMS $= \sqrt{2}$ RMS$_{\text{min}} = 0.00017$, projected onto k_{pyro}. Black dots mark the parameters values that were simulated.

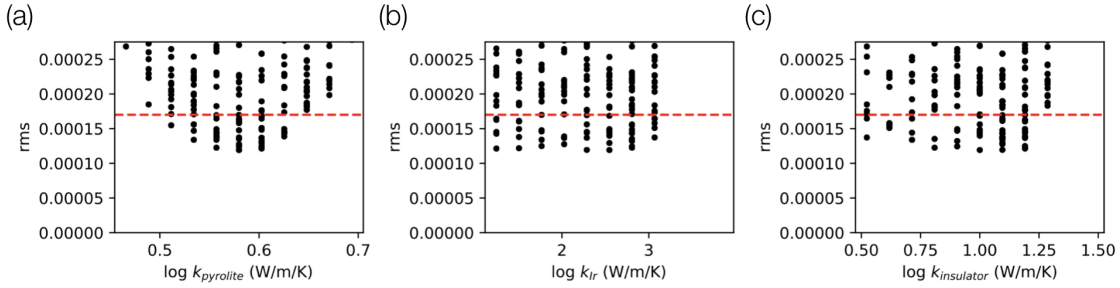

Figure S12: Rms deviations projected onto each axis of free parameter space, $\mathbf{k} = (k_{\text{pyro}}, k_{\text{ins}}, k_{\text{coupler}})$. Red dashed lines mark RMS $= \sqrt{2}$ RMS$_{\text{min}} = 0.00017$.

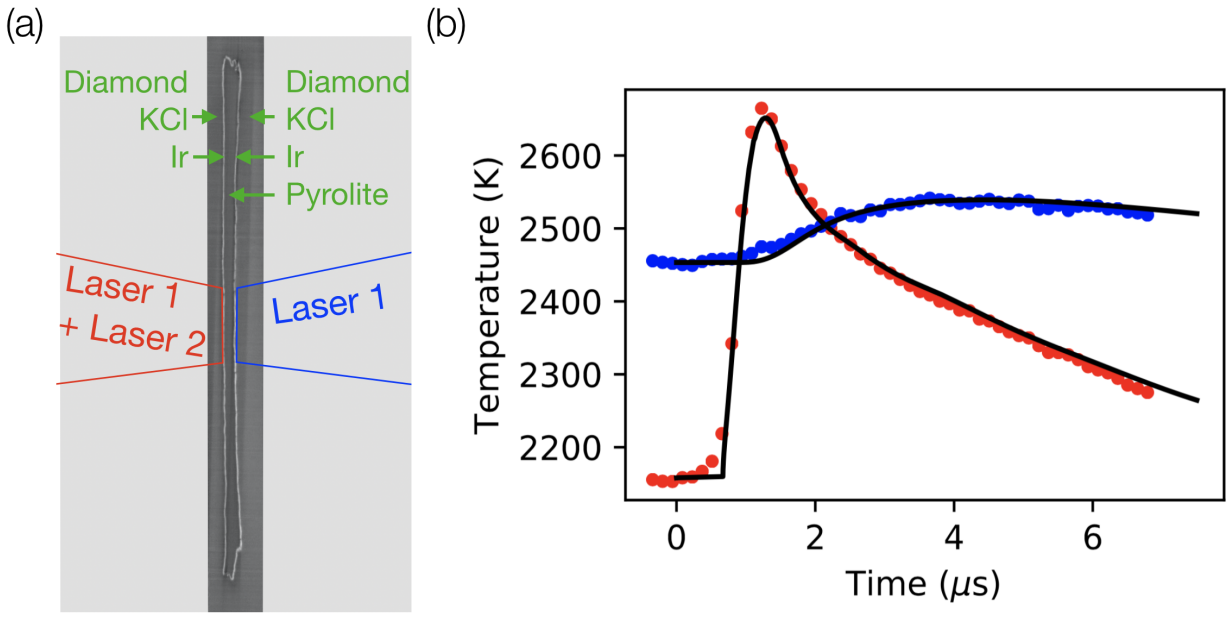

Figure S13: Graphical Abstract: (a) Schematic cross-section of experimental setup, including electron backscatter image of sample recovered from high pressure and sliced in half. The pyrolite sample is coated, insulated, and compressed to 80 GPa in a diamond anvil cell. Lasers 1 and 2 are continuous and pulsed lasers, respectively, which heat the pyrolite sample to the temperature of interest. (b) Measured temperature evolution from left side (red) and right side (blue) at 80 GPa during the heating experiment represented in (a), along with modeled temperature evolutions (black).